1949

Investigation of Noisy Character of Phase Transformations in Ferromagnetic Shape Memory Materials

Thesis for the Degree of Doctor of Philosophy (PhD)

Nora Samy Sdky Mohareb

Supervisor

Prof. Dr. Dezső L. Beke

UNIVERSITY OF DEBRECEN
Doctoral Council of Natural Sciences and Information Technology
Doctoral School of Physics
Debrecen, 2021

Hereby I declare that I prepared this thesis within the Doctoral Council of Natural Sciences and Information Technology, Doctoral School of Physics, University of Debrecen in order to obtain a PhD Degree in Natural Science at Debrecen University.

The results published in the thesis are not reported in any other PhD theses.

Debrecen, 2021.06.15

. . . . . .

Nora Samy Sdky Mohareb

Candidate

Hereby I confirm that Nora Samy Sdky Mohareb candidate conducted her studies with my supervision within the Solid State Physics and Material Science Doctoral Program of the Doctoral School of Physics between 2017 and 2021. The independent studies and research work of the candidate significantly contributed to the results published in the thesis.

I also declare that the results published in the thesis are not reported in any other theses.
I support the acceptance of the thesis.

Debrecen, 2021.06.15

. . . . . .

Prof. Dr. D.L. Beke

Supervisor

Investigation of Noisy Character of Phase Transformations in Ferromagnetic Shape Memory Materials

Dissertation submitted in partial fulfilment of the requirements for the doctoral (PhD) degree in **Physics**

Written by **Nora Samy Sdky Mohareb** certified MSc in Physics

Prepared in the framework of the Physics Doctoral School of the University of Debrecen
(Solid State Physics and Material Science programme)

Dissertation advisor: **Prof. Dr. Dezső L. Beke**

The official opponents of the dissertation:

Dr. ...…… ……..……...
Dr. …...…… …….

The evaluation committee:

Chairperson: Dr...…… ……....
Members: Dr. …… ……
Dr. …… ……
Dr. ……. ……
Dr. ..…… ……

The date of the dissertation defense: 202…….

Contents

List of symbols and abbreviations

SMA	Shape memory alloy
SIM-aging	Stress-induced martensite stabilization
MT	Martensitic Transformation
SME	Shape memory effect
TWSME	Two-way shape memory effect
A	Austenite
M	Martensite
A/M	Austenite transforms to martensite (forward)
M/A	Martensite transforms to austenite (reverse)
p	Atmospheric pressure
ΔG	Total change of Gibbs free energy
G_{nc}	Non chemical Gibbs free energy
G_c	Chemical Gibbs free energy
G_c^A	Chemical Gibbs free energy of austenite
G_c^M	Chemical Gibbs free energy of marteniste
ΔU_c	Internal energy change of the transformation
ΔS_c	Entropy change of the transformation
D	Dissipative energy
E	Elastic energy
T	Temperature
ξ	Martensite Volume Fraction
T_o	Equilibrium transformation temperature
ΔG_M	Driving force for phase transformation at the martensite starts temperature during undercooling ($\Delta G_M = G^A - G^M \sim T_o - M_s$).
M_s	Martensite start temperature
M_f	Martensite finish temperature

A_s	Austenite start temperature
A_f	Austenite finish temperature
Δg_c	Derivative of chemical Gibbs free energy by ξ
$d(\xi)$	Derivative of the dissipative energy by ξ
$e(\xi)$	Derivative of the elastic energy by ξ
Δu	Derivative of the ΔU_c by ξ
Δs	Derivative of the ΔS_c by ξ
σ	Stress
V	Volume
ε_{tr}	Transformation strain
$\sigma_o(0)$	Equilibrium transformation stress at T=0
MFIS	Magnetic Field Induced Strain
$P(X)$	Probability density function of X (which can be e.g. the energy, amplitude, duration time, area)
ρ	Exponent
X_c	Cut-off value
DSC	Differential Scanning Calorimeter
E_i	Energy of the i^{th} peak in DSC
$\varphi(t)$	Amplitude of the peak (heat flux) in DSC
D_i	Duration time of the peak in DSC
τ_{DSC}	Time constant of the exponential decay of a DSC signal
AE	Acoustic Emission
ME	Magnetic Emission
R	Reference electrical resistance (1MΩ)
i	Number of the AE event
j	Number of oscillations in i-th event ($1 \leq j \leq n_i$)
n_i	Total number of oscillations
t_i	Duration time of acoustic event
f	Characteristic frequency of the oscillations ($n_i/2t_i$)

τ_i	Duration time of one oscillation ($\tau_i \cong t_i/n_i$)
u_{ij}	Maximum voltage of the oscillation
S_i	Area of the magnetic signal
t_o	Start of the avalanche
t_f	Finish of the avalanche
C_v	Specific heat capacity
Q	Heat for phase transformation
m	Mass of the sample
n	Numbers of turns of coil
I	Alternating Current
H	Magnetic field strength
U_2	Induced voltage in the secondary coil
U_{20}	Amplitude of the voltage induced in secondary coil
μ	Permeability
Φ	Induction flux in the sample
A	Cross section area of the sample
ML	Maximum likelihood method
X_{min}	The smallest data for the performed evaluation
ε	Energy exponent
α	Amplitude exponent
B	External magnetic field
N	Number of hits
E_t	Sum of peak energies ($\sum_i E_i$)
E_{av}	Average peak energy ($\sum_i E_i$) $/N$
σ_{cr}	Critical stress
$\propto$	Reciprocal of the molar volume
V_M	Molar volume
$\partial e^{\uparrow\downarrow} / \partial \xi$	Second derivatives of the elastic energy by ξ
S_H	Overall shift of the hysteresis
ΔW_H	Change of the area of hysteresis

Introduction

Shape memory alloys (SMAs) are in the focus of scientific and technical interest in recent years since they form a group of smart, functional metallic materials. The functionalities arise from their microstructural changes when subjected to external stimuli like temperature, mechanical stress, or magnetic field changes. SMAs demonstrate unique properties, like shape memory effect and superelasticity. Thus, SMAs are popular for a lot of applications like sensing, actuation, impact absorption, medical implants, and vibration damping.

Investigation of the nature of jerky character of structural transformations (martensitic transformation between austenite and martensite phases or rearrangement of martensite twin variants by twin boundary motions) in shape-memory materials is currently an active area: the motion of the interfaces has intermittent (stop-and-go) character. This intermittent process is characterized by the emission of avalanches/noise signals, which can be thermal, acoustic, or magnetic signals if one of the two phases is ferromagnetic. These avalanches can be described by power law distribution with cutoff. The exponents are universal for a certain range of materials, structural changes, and types of noises, forming so-called universality classes. Noise measurements are relatively new and better methods to study the phase transformations of SMAs. The details of the characteristics of noises can be especially important in understanding of the properties of high performance magnetic SMAs.

In my research, the basic aim was to investigate and analyze different (thermal, acoustic, and magnetic) noises emitted during martensitic transformations in ferromagnetic SMAs. I performed noise measurements on two different SMAs, which are recently very promising in applications:

1) $Ni_{45}Co_5Mn_{36.6}In_{13.4}$ Single Crystals:

In Ni-Co-Mn-In alloys, there is a large difference between the saturation magnetization of the martensite and austenite and thus they are called meta-magnetic SMA. In metamagnetic materials, an external magnetic field can also initiate the martensitic phase transformation, and these alloys can demonstrate high actuation stress levels. They are also very promising for magnetic refrigeration applications, at room temperature, based on the magnetocaloric effect (i.e. when a sudden change of the magnetic order can lead to production or absorption of heat). There were many studies about the properties of these meta-magnetic $Ni_{45}Co_5Mn_{36.6}In_{13.4}$ single crystals, but there was no study for the discontinuous character of the martensitic transformation. We were interested in answering the following questions:

- How the large jump in the magnetization affects the jerky character during the transformation in the different signals (thermal, acoustic, and magnetic)?
- How the behaviour and the exponent of the different signals emitted during the transformation can be affected by the external magnetic field?

Therefore, our aim was to investigate thermal, acoustic, and magnetic signals emitted during the meta-magnetic transition between the ferromagnetic (austenite) and very weakly magnetic (martensite) phases at different values of a constant external magnetic field.

2) $Ni_{51}Fe_{18}Ga_{27}Co_4$ Single Crystals:

Martensite aging can lead to a significant improvement of the shape memory functional properties. It was shown that stress-induced martensite stabilization (SIM-aging: stabilization of a given martensite variant produced by uniaxial stress) results in a large reversible two-way shape memory behavior at higher temperatures. These materials,

due again to the preference of a certain martensite variant, can also show large superelastic deformation or rubber-like behavior (up to about 10-14%) in a martensitic state under the application of unidirectional stress or magnetic field.

There was no study for the discontinuous character of the martensitic transformation due to the SIM-aging effect. We were interested in answering the following questions, which were not studied in the literature:

- How the SIM-aging affects the discontinuous character during the transformation? Does the exponent change?
- Does the entropy of the transformation change due to the SIM-aging effect?

Therefore, my aim was to understand the details of the intermittent character of martensitic transformation due to SIM-aging effect. We carried out a comparative investigation of the change of acoustic emissions characteristics and transformation temperatures as well as the transformation entropy for three states of this alloy; (quenched, austenite stabilized, and martensite stabilized by SIM-aging).

Chapter 1

Literary Antecedents

In this chapter, I will briefly review the literature related to my doctoral research. I will discuss the shape memory alloys and martensitic transformation, ferromagnetic and metamagnetic shape memory alloys, martensite stabilization and then present the physical origins of different noise packages associated with the intermittent character of martensitic transformations.

1.1 Shape Memory Alloys

As it was already mentioned in the introduction, shape memory alloys (SMAs) are in the focus of scientific and technical interest in recent years since they form a group of smart, functional materials [1]–[6]. The functionalities arise from their microstructural changes when subjected to external stimuli like temperature, mechanical stress, or magnetic field changes.

The basic property of all shape memory alloys is the martensitic transformation (MT), during which their phase change involves a cooperative, diffusionless rearrangement of atoms within the crystal lattice [4]. SMAs demonstrate unique properties like shape memory effect (SME), superplasticity, and superelasticity. The so-called two-way shape memory effect (TWSME) is a cyclic shape change upon heating and cooling, while the superelasticity (or pseudoelasticity [2], [3]) is a reversible shape change during stress-induced martensitic transformation. In addition, these materials can show large superelastic deformation or rubber-like behaviour (up to about 10-14%) in a martensitic state under the application of unidirectional stress or magnetic field [7], [8]. Thus, SMAs are popular for a lot of applications like sensing, actuation, impact absorption, medical implants, and vibration damping [3].

1.1.1 Martensitic transformation

As I mentioned earlier, the MT is a diffusionless phase transformation in solids, in which the re-arrangement of atoms often takes place by a shear-like mechanism as shown in Fig. 1.1. Usually, the high-temperature austenitic phase, A, is cubic, and the martensitic one (the lower temperature phase, M) has a lower symmetry (tetragonal, orthorhombic, or monoclinic) [4]. The MT starts when the sample is cooled down below a critical temperature. The martensites in regions A and B have the same structure, but different orientations relative to the parent phase called "variants". Due to the lower symmetry of the martensite, many variants can be formed from the austenite during cooling. If, after deformation in a martensitic state, the temperature is increased the reverse transformation occurs, and the martensite reverts to the parent phase restoring the original shape. This is the origin of SME [5].

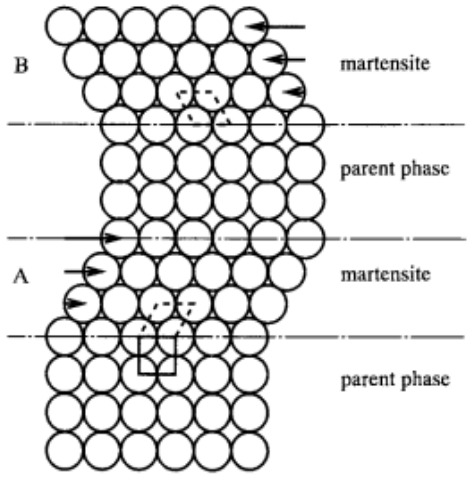

Figure 1.1 Schematic figure of the martensitic transformation [5].

The formed martensitic phase can have a different type of variants [4]:

- "Self-accommodated martensite variants": randomly oriented multivariant martensite develops with small or negligible net

shape change by cooling the austenite (the first step in Fig. 1.2) in the absence of an external field.

- "Single variant martensite": with a specific variant being dominant having a visible shape change under the effect of stress (second step in Fig. 1.2), or magnetic field if the SMA is ferromagnetic.

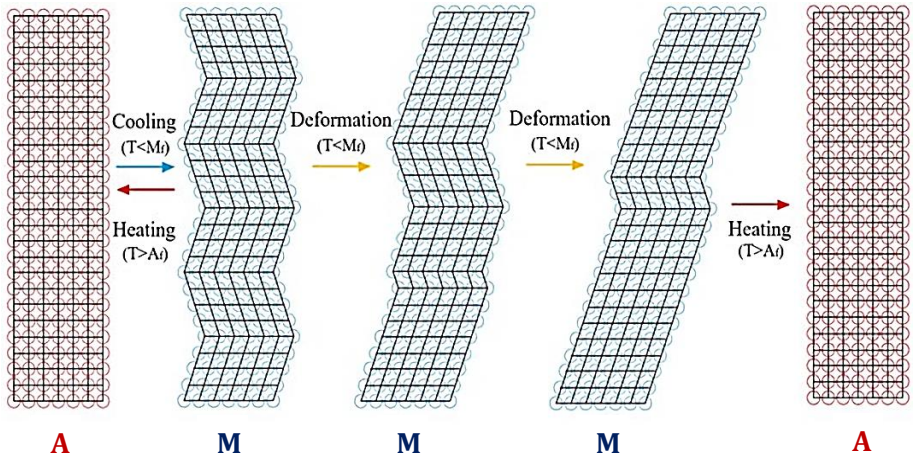

Figure 1.2 Phase and shape change during martensitic transformation (one way shape memory effect) [9].

Since MT is a first-order transformation, it proceeds by nucleation and growth. Since MT is always associated with a shape change, when a martensite nucleus is formed in the austenite, a large strain field can arise around it. The tendency (due to the constrain of keeping the original macroscopic shape during the growth of martensite nuclei) to reduce the strain/stress field is essentially important in the nucleation and growth processes. There are two ways to attain it: either by a slip or by twins as shown in Fig. 1.3: these are called lattice invariant shears [5].

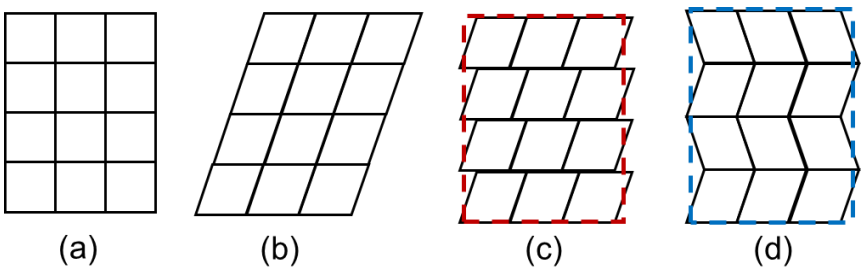

Figure 1.3 Schematic diagram for the formation of a martensite nucleus: (a) austenite crystal, (b) homogeneous lattice deformation would be accompanied with the formation of the martensite. The dashed horizontal lines indicate that there is a constrain by the surrounding matrix to keep the original macroscopic shape of the austenite. The martensite should fit in the dashed area, by introducing slip (c) or by twinning (d).

1.1.2 Thermodynamics of martensitic transformation

The temperature dependence of the chemical Gibbs free energies of the two phases can be illustrated as shown in Fig. 1.4. The total change of the Gibbs free energy includes the chemical and nonchemical terms (the nonchemical terms, i.e. the elastic and dissipative energy contributions too). For the down A/M transformation the total change of the Gibbs free energy at atmospheric pressure and zero stress (i.e. at $p \cong 0$ and $\sigma = 0$) can be given by:

$$\Delta G^{\downarrow} = G^{M} - G^{A} = \Delta G_c^{\downarrow} + \Delta G_{nc}^{\downarrow} = \Delta G_c^{\downarrow} + \left(D^{\downarrow} + E^{\downarrow}\right) \tag{1.1}$$

$$\text{and} \quad \Delta G_c^{\downarrow} = \mathrm{G}_c^{M} - G_c^{A} = \Delta U_c^{\downarrow} - T\Delta S_c^{\downarrow}, \tag{1.2}$$

where the chemical Gibbs free energies of martensite (M) and austenite (A) phases are G_c^M and G_c^A. $\Delta U_c^{\downarrow}$ and $\Delta S_c^{\downarrow}$ denote the change of the internal energy and entropy, respectively. D and E denote the dissipative and elastic energy, respectively. Similar expressions can be written for the up (M/A) transformation as well. The dissipative energy

arises from the frictional motion of the interfaces, while the elastic energy accumulates during the A/M transformation because of the overlapping of elastic fields of the different martensite nuclei and/or variants (due to the transformation strain). This accumulated elastic energy is released during the M/A transformation. Thus it is positive for the A/M transformation and negative for the reverse direction. On the other hand, the dissipative energy is positive in both directions [10], which also means that there is a hysteresis on the $\xi(T)$ function taken on a heating/cooling cycle (ξ is the martensite volume fraction: $0 \leq \xi \leq 1$). Since the energy of nucleation is also always positive in both directions, this additional term can be considered as it would be included in D [10].

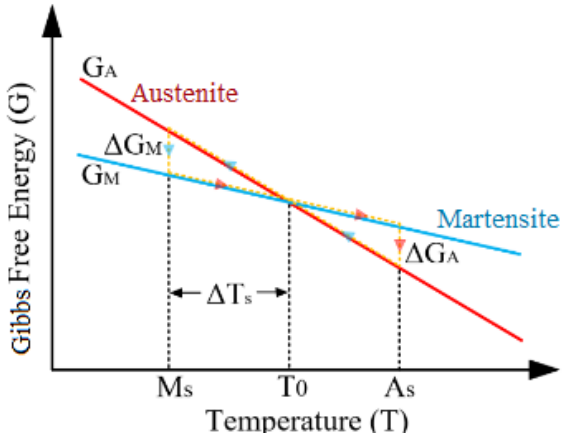

Figure 1.4 The chemical Gibbs free energies as the function of temperature and the equilibrium transformation temperature (T_o) (e.g. ΔG_M is the driving force for phase transformation at the martensite start temperature during undercooling, i.e. $\Delta G_M = G^A - G^M \sim T_o - M_s$) [9].

Assuming a local equilibrium approach [10] during the transformation, $\frac{\partial \Delta G^{\downarrow}}{\partial \xi}$ should be equal to 0 (at any ξ or T value):

$$\frac{\partial \Delta G^{\downarrow}}{\partial \xi} = \frac{\partial (\Delta G_c^{\downarrow} + D^{\downarrow} + E^{\downarrow})}{\partial \xi} = \Delta g_c^{\downarrow} + d^{\downarrow}(\xi) + e^{\downarrow}(\xi) = 0, \qquad (1.3)$$

where the small letters are the derivatives of the corresponding energy terms. It is assumed that $\Delta g_c^{\downarrow}$ is independent of ξ (i.e. $\Delta G_c^{\downarrow}$ is proportional to ξ):

$$\Delta g_c^{\downarrow} = \Delta u_c^{\downarrow} - T\Delta s_c^{\downarrow} \tag{1.4}$$

The temperature belonging to $\Delta g_c^{\downarrow} = \Delta g_c^{\uparrow} = 0$ is the equilibrium transformation temperature T_o:

$$T_o = \frac{\Delta u^{\downarrow}}{\Delta s^{\downarrow}} = \frac{\Delta u^{\uparrow}}{\Delta s^{\uparrow}} \tag{1.5}$$

($\Delta u^{\downarrow}(< 0) = -\Delta u^{\uparrow}$ as well as $\Delta s^{\downarrow}(< 0) = -\Delta s^{\uparrow}$). The martensite start, M_s, and finish, M_f, temperatures can be defined by taking Eq. 1.3 equal to zero for ξ = 0 as well as ξ =1, respectively. In general, the $T^{\downarrow}(\xi)$ curve, defined by taking Eq. 1.3 equal to zero at arbitrary ξ, gives the lower part of the hysteresis curve (i.e. the $\xi(T^{\downarrow})$ curve). Similarly the $\xi(T^{\uparrow})$ curve, for the M/A transformation (with ↑ arrow), is the upper branch of the hysteresis curve. Thus

$$T^{\downarrow}(\xi) = T_o + \frac{e^{\downarrow}(\xi)+d^{\downarrow}(\xi)}{\Delta s^{\downarrow}} \tag{1.6a}$$

and

$$T^{\uparrow}(\xi) = T_o + \frac{e^{\uparrow}(\xi) + d^{\uparrow}(\xi)}{\Delta s^{\uparrow}}, \tag{1.6b}$$

while the inverses of Eqs. (1.6a) and (1.6b), are the down and up branches of the hysteresis loops. The shape of the hysteresis curves are shown in Fig. 1.5 for the following schematic cases [10]:

a) Both $d(\xi)$and $e(\xi)$ are zero; the transformation takes place at T_o, in both directions.
b) $e(\xi)$ =0 and $d(\xi)$ ≠0, and $d(\xi)$ is constant; the $\xi(T^{\downarrow})$ and $\xi(T^{\uparrow})$ branches are vertical and there is already a hysteresis.
c) $d(\xi)$ is constant and $e(\xi)$ linearly depends on ξ; the hysteresis curve is tilted, reflecting the ξ dependence of e.

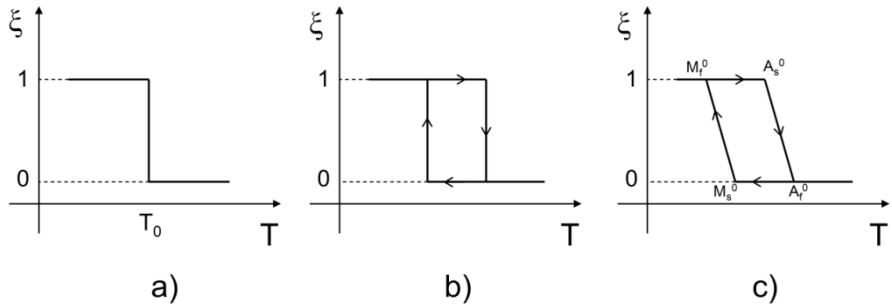

Figure 1.5 Schematic thermal hysteresis loops [10].

The area of the hysteresis loop corresponds to the dissipated energy during one cycle, $2D$ (if one assumes that $E^{\downarrow} = -E^{\uparrow}$: see also below):

$$2D = \int_o^1 \Delta s^{\downarrow}(T^{\downarrow}(\xi) - T^{\uparrow}(\xi))d\xi = \int_o^1 (d^{\downarrow}(\xi) + d^{\uparrow}(\xi))d\xi. \qquad (1.7)$$

(It is often assumed that $D_1 = \int_o^1 (d^{\downarrow}(\xi)d\xi = D_2 = \int_0^1 d^{\uparrow}(\xi)\, d\xi = D$). It is clear from Fig. 1.4, and Eq. (1.3) that for cooling below T_o (here ΔG_c is negative and both $D$and E are positive), ΔG will be zero at a certain temperature, where the sum of the differences of the chemical and non-chemical terms is zero. The particle formed during cooling at this temperature can grow further or become smaller only by undercooling or overheating, respectively (balance between the chemical and non-chemical terms). For $d(\xi)/dT$=const. this is in fact the thermoelastic balance since in this case, the elastic and chemical terms will be "balanced" (see Figs. 1.4 and 1.5c). Undercooling or overheating increases the driving force of the transformation (i.e. the difference of Gibbs-free energies: see Fig. 1.4).

If $\sigma \neq 0$, then the additional term $(-\sigma V \varepsilon_{tr}^{\downarrow})$ appears on the right-hand side of Eq. (1.4) [10] (V is the volume and $\varepsilon_{tr}^{\downarrow} = -\varepsilon_{tr}^{\uparrow}$ is the transformation strain) and thus one gets:

$$T_o(\sigma) = T_o(0) + \sigma V \frac{\varepsilon_{tr}^{\downarrow}(\sigma)}{\Delta s^{\downarrow}} \tag{1.8}$$

as well as

$$\sigma_o(T) = \sigma_o(0)\frac{\varepsilon_{tr}^{\downarrow}(T)}{\varepsilon_{tr}^{\downarrow}(0)} - \frac{T\Delta s^{\downarrow}}{V\varepsilon_{tr}^{\downarrow}(T)} = [T_o(0) - T]\frac{\Delta s^{\downarrow}}{V\varepsilon_{tr}^{\downarrow}(T)} \tag{1.9}$$

Here $\sigma_o(0) = \frac{\Delta u_c^{\downarrow}}{V\varepsilon_{tr}^{\downarrow}(0)}$ is the equilibrium transformation stress at T=0. It can be seen, that these are the well-known Clausius-Clapeyron relations [10] and they are linear if $\varepsilon_{tr}(\sigma)$ as well as $\varepsilon_{tr}(T)$ are constants.

1.1.3 Properties of shape memory alloys

For the one-way shape change, shown in Fig. 1.2, an externally applied stress is necessary to induce a large shape change in a martensitic state (second step in Fig. 1.2) which can be recovered to the original shape upon heating (last step in Fig. 1.2).

Thus, in “pure” one-way SME, during cooling of the austenite, there is a transformation to multivariant martensite by self-accommodating growth of different variants and the average macroscopic strain is practically zero during cooling (OA path in Fig. 1.6). Then, uniaxial stress is applied, resulting in the reorientation of the variants and the development of a single martensite variant structure with large inelastic strains (AB path). Upon unloading (along BC), the material remains in this state with unrecoverable strain. Finally, when it is heated above A_f, the SMA returns to its cubic austenite (C0) and the inelastic strains are recovered [11], [12]. It can happen, however (i.e. by preferred nucleation of one of the variants) that the strain is not zero both during heating and cooling. Then this property is known as two-way shape memory effect (TWSME) and it was observed for the first time by Perkins (1974).

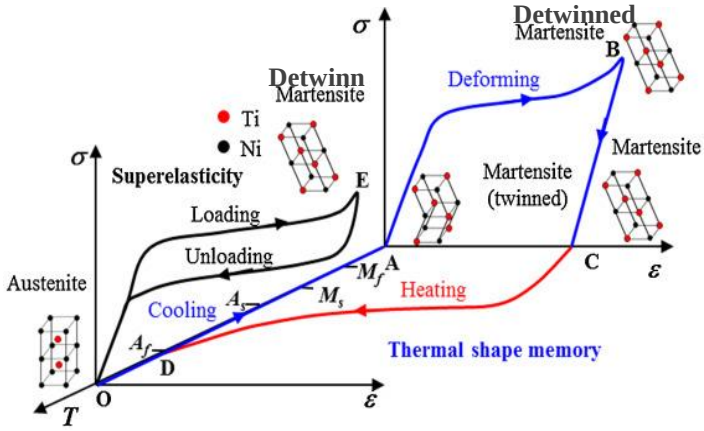

Figure 1.6 Shape memory effect and pseudoelasticity of typical SMA [13].

In pseudoelasticity or superelastic behavior, when the austenite (point 0) is loaded, there is only an elastic deformation up to a critical transformation stress level, σ_{Ms}, at which the formation of martensite starts. Above this stress level, a stress-induced A/M phase transformation starts and results in single variant martensite (point E) with a large transformation strain. During the reverse transformation (M/A), the original shape is recovered.

In contrast with the one-way SME and superelasticity, the TWSME is not an intrinsic but an acquired characteristic. It describes the ability of a material to remember two different shapes and the temperature-induced transition between them is obtained without any applied stress assistance. TWSME can be attained by the cyclic repetition of certain thermo-mechanical treatments [14], by training, to learn the sample to nucleate preferably one variant. From the application point of view, TWSME enables the enhancement of the functionality of the working element from the SMAs in the engineering of actuators [14]. Recently the stress-induced martensite stabilization (SIM-aging) provides an especially effective way to produce the preference of one variant and this enhances both the TWSME and the rubber like-behavior [7], [8] in a martensitic state. We will describe the details of stress-induced martensite stabilization in the next section.

1.2 Martensite Stabilization

Stress-induced martensite stabilization (SIM-aging) heat treatments are carried out under uniaxial stress. The stress and the temperature should be large enough to produce single variant martensite as well as allow atomic diffusion, respectively in SMAs [8], [15]–[20]. SIM-aging results in two effects, due to the stabilization of the given martensite variant: i) increases the reverse transformation temperature (A_f), ii) enhances the "rubber-like behavior", in which the martensite turns back to its original shape if it deformed in a martensitic state [21] (as shown in Fig. 1.7 for the stabilized martensite by SIM-aging). SIM-aging causes a significant improvement of the shape memory functional properties [15]–[20], since both the TWSME and rubber-like behaviour in the martensitic state can be extended almost up to the maximal possible values of the formation strains and/or reorientation strains between two variants [21], [22].

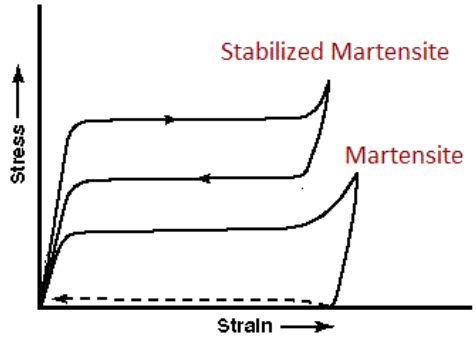

Figure 1.7 Schematic stress-strain curves for fresh martensite (superplasticity) and stabilized martensite (rubber-like behavior).

This martensite stabilization is based on the so-called symmetry conforming short-range ordering process [19], [22]. Both the martensite and austenite have chemically ordered atomic structure and in the austenitic state, this chemical order fully conforms to the high symmetry austenite crystalline structure. During aging in a martensitic state, there is a short-range reordering of atoms to accommodate the

chemical order according to the martensite crystal symmetry (see Fig. 1.8).

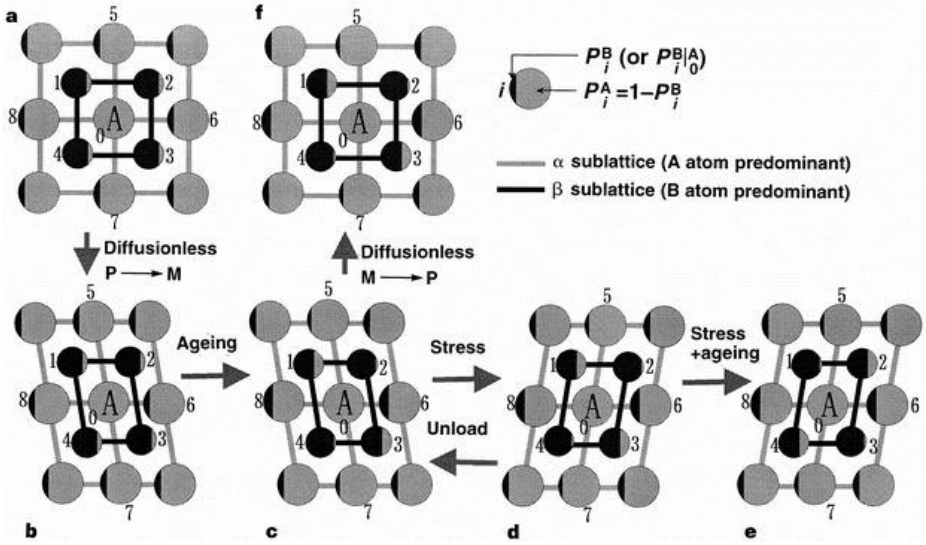

Figure 1.8 Mechanism of symmetry-conforming short-range ordering. The conditional probabilities around an A-atom are shown in an imperfectly-ordered A-B alloy: (a) in the equilibrium parent austenite; (b) in the martensite, immediately after transformed from (a); (c) in the equilibrium martensite; (d) in the stress-induced martensite domain (twin) immediately formed from (c); (e) in the stress-induced domain in equilibrium state; and (f) in parent transformed from (c), respectively. P and M denote the austenite and martensite, respectively. P_i^B (or P_i^A) is the probability of B atom (or A atom) occupying i-site (i= 1,2,…,8) if an A atom is at 0-site. The black and grey areas show the relative values of P_i^B and P_i^A respectively [21].

It was shown in a very recent paper [8] that in $Ni_{51}Fe_{18}Ga_{27}Co_4$ single-crystal not only the TWSME (with a reversible tensile strain of 9%) was improved, but giant rubber-like behavior (up to 15%) during reorientation of martensite variants was also achieved by SIM-aging. This is about twice larger than the maximum transformation strain during the B2-$L1_o$ A/M transformation.

1.3 Meta-Magnetic Shape Memory Alloys

Meta-magnetic SMAs are alloys in which an external magnetic field can also induce shape change. This is the magnetic field-induced strain, MFIS [23]–[26]. Usually, in these alloys the austenite is ferromagnetic and the martensite is weakly magnetic, and the second-order magnetic transition and the first order martensitic transformation overlap. The shape change induced by the magnetic field can be two types:

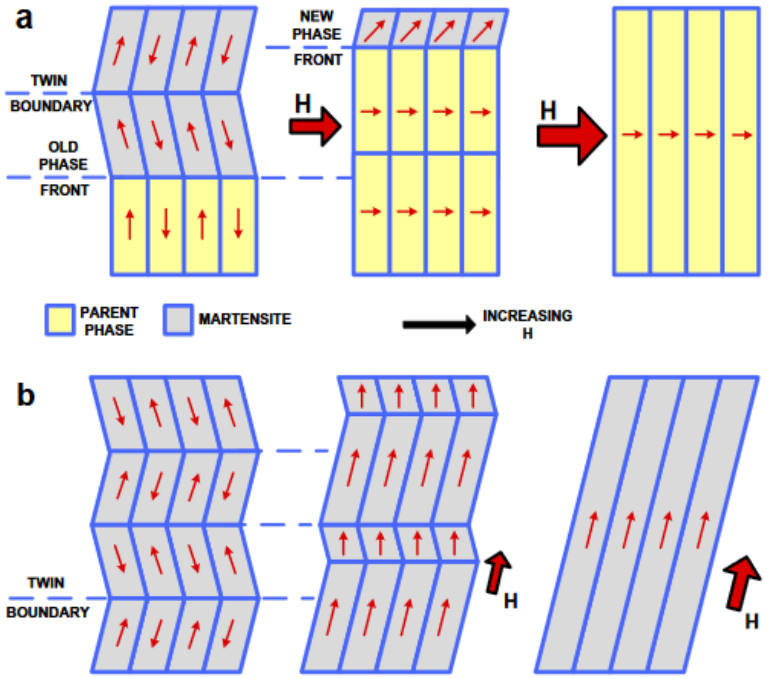

Figure 1.9 Schematic figures to show the MFIS in magnetic SMAs under the magnetic field effect H [25].

a. Shape change during phase transformation [25]: this mechanism is similar to stress- or temperature-induced MT. The driving force of this mechanism to move the phase front between the two phases is the magnetic anisotropy energy as well as the Zeeman energy [27], [28]. The Zeeman energy originates from the difference of the saturation magnetizations

of the two phases and it is proportional to the field, as shown in Fig. 1.9a.

b. Shape change during twin reorientation in the martensitic state [24]: the external magnetic field initiates the growth of twins with preferred orientation (with easy axis parallel with the field direction) at the expense of others, which leads to a shape change and development of a mono-variant twin structure (Fig. 1.9b). To obtain a reversible shape change, application of external stress (to change back the variant structure) is required.

High magnetocrystalline anisotropy energy and low energy of twin boundary motion [24] are required for the mechanism (b), so at present, it is limited to single crystals. Since the Zeeman energy is independent of the crystal orientation, mechanism (a) offers also the use of polycrystals for actuators [28].

The huge difference between the magnetization of austenite and martensite makes these materials be promising for magnetic refrigeration applications, at room temperature, based on the magnetocaloric effect [29]–[31] too. During the magnetic field-induced first-order phase transformation of the ferromagnetic austenite into weak magnetic martensite, a significant latent heat can be obtained, which is beneficial for such applications. Recently, the Ni-Co-Mn-In system as a meta-magnetic SMA is very promising for such applications.

1.4 Noise Emission during Martensitic Transformation

Systems can respond to a slow external driving force by crackling noise, characterized by the emission of avalanches or pulses of corresponding signals in a broad range of sizes. There is a wide range of phenomena showing such behaviour, like the crumpling of papers, earthquakes, Barkhausen noise, acoustic signals during plastic deformation and fracture, etc.

The motion of phase boundaries during martensitic transformations usually has a jerky or an intermittent (stop-and-go) character. Similarly, the rearrangements of martensite variants also have a jerky character. During such discrete jumps of the boundaries, there is always a sudden strain change, which can lead to the emission of acoustic waves, and the signals have a self-similar behavior: they show the same statistical properties at many scales. Besides, it is possible to detect the emission of magnetic noises too, if there are abrupt changes in magnetization [32], [33] during the structural changes.

The avalanches of the noise signals, emitted during the above self-similar, jerky motion of interfaces can be generally described by a power law distribution with cut-off (damped power law; the avalanche statistics is damped) [34], [35]:

$$P(X) = X^{-\rho} e^{(-X/X_c)} ; \tag{1.10}$$

where $P(X)$ is the probability density function of X, X can be the size, energy, amplitude, or duration of the signals, ρ is the power exponent, and X_c is the cutoff value in the second factor describing the damping behaviour. The exponents are denoted by α and ε, for the amplitude and energy, respectively. It was shown in [36] that the value of exponents in (1.10) depends on the crystal symmetry change during the phase transformation.

However, it was observed that the exponents were a bit different for different microstructural length scales (e.g. in alloys with and without nano-precipitates [37]). Similarly, the exponents could be different even for heating and cooling [38]. Therefore, the statistical analysis of different noises emitted during interface motions can provide information on the fundamental physics behind the martensitic transformation, or martensite variant reorientation. For instance, in [38], the difference of the noise activities (and the corresponding exponents) for the austenite to martensite as well as reverse transformations was explained by the possible ways of relaxations of the elastic strain energy.

1.4.1 Thermal Emission

The first-order martensitic transformation is accompanied with the release/absorption of latent heat. The transformation temperatures and the heat of transformation can be determined by Differential Scanning Calorimeter (DSC). Fig. 1.10 shows the power (mW) required to maintain a constant heating or cooling rate versus the temperature, i.e. a typical DSC curve for SMA specimen. Heating the specimen, the transformation to austenite initiates at A_s. During the reverse transformation, in order to maintain the prescribed heating rate, the endothermic reaction requires additional heat power to be supplied to the specimen. This is recorded as a transformation "peak" during heating. Similarly, for exothermic reaction during cooling, a peak of opposite sign is recorded. The transformation temperatures are usually determined by the intersection of tangents fitted to the start and end regions of the transformation peak and the baseline of the heating and cooling curves [3].

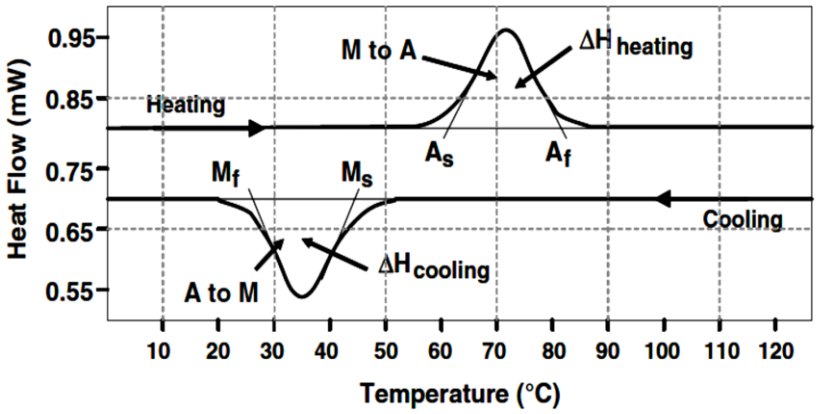

Figure 1.10 Typical DSC curve for SMAs [3].

At usual fast scanning rates, an integrated peak of latent heat appears hiding the fine structure of the jerky character of transformation. The corresponding fine structure can be observed under lower scanning (driving) rates. Indeed, for slower scanning rates (in the order of 0.1 K/min), the envelope peak can be split into individual

peaks, making possible the determination of the power exponents, characterizing the probability density function of the energy of individual peaks. The surface roughness and the mass of the sample are also important parameters in optimizing the best signal/noise ratio [39]. For illustration, Fig. 1.11 shows the thermal noise for our investigated $Ni_{45}Co_5Mn_{36.6}In_{13.4}$ sample at 0.3 K/min (see also below).

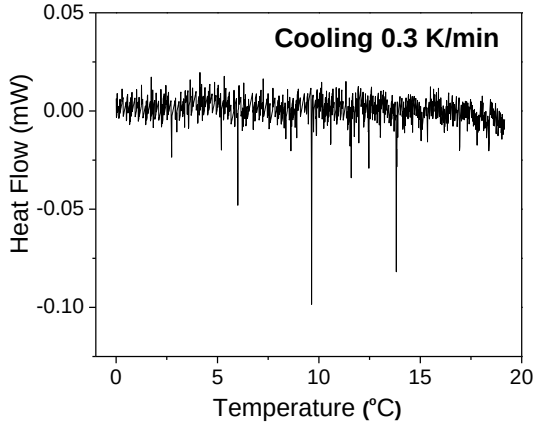

Figure 1.11 Thermal noises in $Ni_{45}Co_5Mn_{36.6}In_{13.4}$ single crystal SMA during cooling at 0.3 K/min.

For a separate peak, integrating the DSC curve over the duration time of the peak gives the energy of the event. As a consequence of the exponential decay of the DSC signals, the integral is proportional to the magnitude of the peak:

$$E_i = \int_0^{D_i} \varphi(t)dt = \int_0^{D_i} \varphi_{max} \exp\left(-\frac{t}{\tau_{DSC}}\right) dt = -\tau_{DSC}\varphi_{max}\left[e^{-\frac{D_i}{\tau_{DSC}}} - 1\right] \quad (1.11)$$

where E_i is the energy of the i^{th} peak, D_i is its duration time, and φ_{max} is the amplitude of the peak (heat flux). Assume, as it was done in the Gallardo's paper [40], that the time constant of the exponential decay of a DSC signal is larger than the characteristic duration time (of the avalanches/separate signals), i.e. $D_i \ll \tau_{DSC}$. Then:

$$E \approx \varphi_{max} D_i \approx \varphi_{max.} \quad (1.12)$$

Here the $e^{-\frac{D_i}{\tau_{DSC}}} \cong 1 - \frac{D_i}{\tau_{DSC}}$ relation was used ($D_i << \tau_{DSC}$).

Thus, to calculate the peak energy distribution, after deducting the decay, it is sufficient to determine only the amplitude of each peak [40].

1.4.2 Acoustic Emission (AE)

As mentioned earlier the acoustic emission is the result of discontinuous displacements of the moving interfaces. It typically occurs in the ultrasonic frequency range between 30 kHz and 1MHz. AE can be observed in many externally stimulated processes associated with rapid changes in the internal strain field, like ferroelastic first-order transitions, dislocation dynamics, stress drops during plastic deformation, or micro-crack propagation [36]. Since the martensitic transitions are accompanied with sudden local changes of the strain field, AE is also observed during these phase transformations. Discussing the reasons for such intermittent behavior, one must consider the following effects [36]:

i) Nucleation of martensite nuclei.
ii) Frictional interactions at the jumping interface: pinning/depinning effects at atomic defects, like dislocations, or at more macroscopic defects (surface roughening, etc.)
iii) Accumulation/relaxation of the stored elastic energy (due to interaction of the different growing/diminishing martensitic variants) can occur.

Each of the above effects can cause a sudden jump of the moving interface. Fig. 1.12 illustrates a typical measured AE signal of one event with medium energy. The AE activity is the number of hits (events), detected during a given time interval. The corresponding event is characterized by two important features; its amplitude, which is the maximum voltage and the duration time of the signal and its energy can be computed approximately as [36]:

$$E_i = \frac{1}{R}\sum_j \frac{u_{ij}^2}{2}\tau_i \tag{1.13}$$

where R is an arbitrary chosen electrical resistance [36], [41] (taken as 1 MΩ), u_{ij}^2 is the amplitude of oscillation, and $\tau_i = t_i/2n_i$, where t_i is the duration time of the event. The length of all small separate triangle-shaped peaks (see the insert in Fig. 1.12) is the same ($2\tau_i$ and n_i denote the duration time and the number of oscillations). The estimated characteristic frequency of the oscillations (using the relation $f = 1/2\tau_i = n_i/t_i$) is in the order of 100 kHz, corresponding to the resonant frequency of the AE sensor.

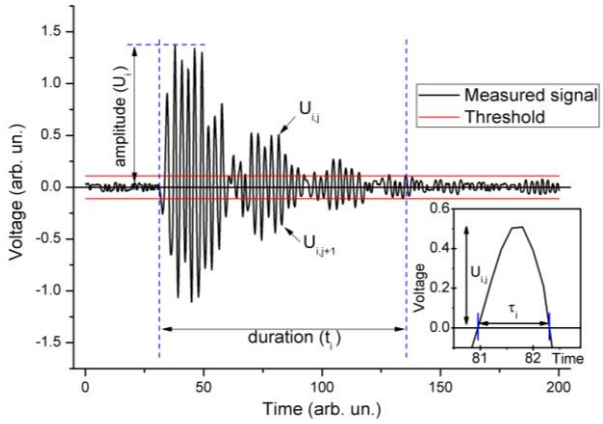

Figure 1.12 AE signal of one acoustic event with medium energy. It can be seen that it contains oscillations of duration $2\tau_i$. One peak in the event is shown in the insert. The index "i" refers to the number of the AE events, while index "j" refers to the number of oscillations within the i-th event, $1 \le j \le n_i$ (see also the text).

Measuring AE with sensitive piezoelectric transducers enables the detection of phenomena occurring at scales from nano to micrometers. AE carries temporal and spatial information about the internal strain field, and this provides valuable information regarding the transformation dynamics [42].

1.4.3 Magnetic Emission (ME)

In magnetic SMAs, the austenite and martensite phases have different magnetic properties and thus during martensitic transformations, large rearrangements of magnetic domains can take place as well. Thus, it is expected that large ME signals (like the classical Barkhausen noises, but different in origin) can be detected [43]. The classical Barkhausen noises can be detected by applying an external magnetic field. The discontinuous jumps in the magnetic domain boundary under increasing magnetic field lead to sharp changes in the magnetic flux, which can be detected, in the form of voltage peaks, V, by winding a coil around the specimen. If the coil is connected to a speaker, crackling noises are heard.

In ferromagnetic SMAs, there are rearrangements in the magnetic domain structure, even in the absence of an external magnetic field, during the MT (or the rearrangement of the martensite variant structure in the martensitic state). In the case of phase transition the nature of such ME signals is influenced by the magnetic properties of both phases. The ME signals have the same origin as AE, however, while AE directly characterizes the velocity of jumps of the habit plane, the ME does it via the magnetoelastic coupling between the magnetic domains and the two phases or martensitic variants [44], [45]: the motion of the interface creates jumps of the magnetic domain walls. These noises can also be characterized by power-law distribution functions with cut-off. We will discuss more details in the next chapter.

The definitions of duration, amplitude, and energy of the magnetic signal are the same as those discussed for acoustic emission. The energy (E_i) of the magnetic signal is proportional to the integral of the square of the voltage signal over the interval [t_0, t_f], duration time [46]:

$$E_i = \frac{1}{R}\int_{t_0}^{t_f} V^2\,(t)dt \tag{1.14}$$

where R is a reference electrical resistance.

Usually, the detected voltage signals are grouped in so-called avalanches: there is an overlap of subsequent signals, which form an avalanche. In the case of ME, the area of the avalanche (the avalanche size) can also be determined [47], which gives the change in magnetic flux during the duration of the avalanche. The area (S_i) of the signals was calculated according to the usual definition:

$$S_i = \int_{t_o}^{t_f} |V(t)|\, dt, \tag{1.15}$$

where t_o and the t_f belong to the start and finish of the avalanche, and T=t_f-t_o is the duration time.

Currently, the study of avalanche critical behavior is an area of intensive research from both theoretical and experimental points of view [44], [45]. The details of the above processes can be very important in the understanding of high performance magnetic SME. Ferromagnetic SMAs are also widely used in such applications, where the shape change is controlled by an external magnetic field. I report, for the first time, noise measurements on the temperature-induced martensitic transformation between ferromagnetic (A) and very weakly magnetic (M) phases in $Ni_{45}Co_5Mn_{36.6}In_{13.4}$ SMA single crystals. Identification of characteristics of AE and ME signals during this meta-magnetic MT can also help in the future applications for structural health monitoring and sensing, as sensory materials [48].

Chapter 2

Experimental Procedures

2.1 Samples

I investigated two different single crystals. The samples were prepared by our partners, in collaboration with Texas and Tomsk Universities in the United States and Russia, respectively. The samples were ready for use for different measurements.

1) $Ni_{45}Co_5Mn_{36.6}In_{13.4}$ single crystal

$Ni_{45}Co_5Mn_{36.6}In_{13.4}$ (at. %) was obtained from Texas University, United States. The sample was prepared by vacuum induction melting of elementally high purity constituents. The Bridgman method under helium atmosphere was used to grow the alloy to get 1.5mm x 1mm x 4cm square rods. The rods, with long axis of the specimen along the [011] direction, were cut using an electrical discharge machine, wrapped in tantalum foil, and placed into a quartz tube (exposed to a high vacuum of ~4 x 10^{-5} mbar for 30 min, and were backfilled with ultra-high purity argon before being sealed). The samples then were heat-treated for 24h at 900 ^{o}C, which was followed by quench in room temperature water, with vigorous stirring and without cracking the quartz tube. Summary of different measurements carried out for this alloy are shown in table 2.1 with the investigated masses and dimensions.

Table 2.1 The different measurements for quenched $Ni_{45}Co_5Mn_{36.6}In_{13.4}$ *single crystals*.

Condition	Mass, dimensions	Tests
Heat-treated at 900 ^{o}C for 24h, followed by quenching in water.	13 mg, 35 mg	DSC
	1.5mmx1mmx4cm square rods	Simultaneous AE and ME and Permeability

2) $Ni_{51}Fe_{18}Ga_{27}Co_4$ single crystal

This alloy was prepared at Tomsk University, Russia. Ingots of $Ni_{51}Fe_{18}Ga_{27}Co_4$ (at.%) alloy were produced by vacuum induction melting. The Bridgman method in a helium atmosphere was used to grow the single crystals. The samples of 3 mm x 3 mm x 6 mm size were annealed at 1373 K for 1 h at temperatures above the order-disorder transition temperature (T = 923–973 K), which was followed by water quench to T=293 K (quenched samples). The high-temperature B2 phase of the quenched crystals transforms to the $L1_0$-martensite. Instron VHS 5969 testing machine (Instron, USA), with $1x10^{-3}$ s^{-1} strain rate, was used for SIM-aging at 423 K under compressive stress. After the formation of the stress-induced monovariant martensite, the sample was kept at this temperature under 400 MPa stress, for 1h along the [110]B2||[100]$L1_0$ direction.

For stabilization of the austenite, heat treatments were carried out at 573 K for 6h below the order/disorder temperature (T= 923–973 K) in the austenitic state followed by slow cooling in furnace.Thus we measured simultaneous DSC and AE for three different states for this alloy (see also Table 2.2).

Table 2.2 Three different states of $Ni_{51}Fe_{18}Ga_{27}Co_4$ *single crystals* for simultaneous DSC and AE measurements.

$Ni_{51}Fe_{18}Ga_{27}Co_4$ Single Crystals	**Condition**	**Mass**	**Tests**
Quenched	Annealed at 1373 K for 1 h, quenched into water.	385 mg	Simultaneous DSC and AE
Austenite Stabilized	Annealed at 1373 K for 1 h, quenched into water + aging at 573 K for 6h followed by slow cooling in furnace.	385 mg	
Martensite Stabilized (SIM-aged)	Annealed at 1373 K for 1 h, quenched into water + SIM-aging (keeping at 423 K, under 400 MPa stress for 1h along [110]B2-direction).	18 mg, 47 mg	

2.2 Experimental Techniques

2.2.1 Differential Scanning Calorimeter

A Perkin Elmer DSC 7 device (Perkin Elmer Inc., USA), with driving rates in the range of 0.3-10 K/min, was used for our DSC measurements. For each different cooling/heating rate, the DSC was calibrated based on the melting points and heat of fusion of pure indium and tin.

Figure 2.1 Perkin Elmer DSC 7 device**.**

Argon gas was flowing during the measurements to prevent oxidization at high temperatures. The DSC was cooled down to -20 ^{o}C by freezing the refrigerant with liquid nitrogen because for some samples the transformation temperatures were low. After freezing, a new calibration was made.

The specific heat capacity can be calculated from the DSC curves by normalizing the heat power by the heating rate and the mass of the specimen ($C_v = (1/m)(dQ/dT)$; where dQ/dT =heat power/driving rate and m is the mass of the sample). Integration of the specific heat between the start and finish transformation temperatures ($\Delta T = T_s - T_f$, $Q = \int_{T_s}^{T_f} C_v dT$) [3], was used to get the latent heat of phase transformation.

The relatively long exponential decay of individual DSC peaks can lead to an overlap of neighboring peak(s) (see Figs. 1.11 and 2.2). Thus, I determined the time constant of the DSC equipment by using a short laser pulse to a calibration sample in isotherm mode, and the time constant (τ_{DSC}=6s) was determined from the response of the device (it is proportional to exp $(-t/\tau_{DSC})$). Thus, I made a correction and the effect of the overlap of the neighboring peaks was removed. The background noise was filtered with a properly chosen threshold value. Before evaluation, baseline correction was also performed on the measured DSC curves.

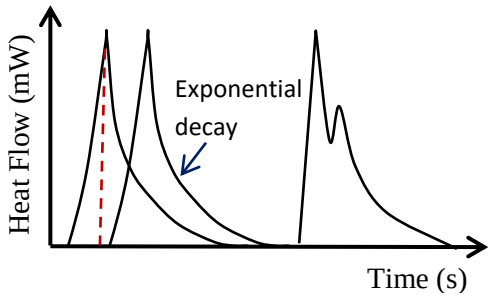

Figure 2.2 Schematic figure shows the exponential decay for the individual peaks in the DSC.

From the analysis of the DSC curves, one can get:

1. The entropy of the transformation

The entropy of the phase transformation can be calculated from the integrals of the cooling down and heating up Q/T curves [10], [49]:

$$\Delta S^{\downarrow} = \int_{M_s}^{M_f} \left(\frac{dQ^{\downarrow}}{T}\right) dT \approx -\int_{A_s}^{A_f} \left(\frac{dQ^{\uparrow}}{T}\right) dT \qquad (2.1)$$

Here Q denotes the heat of the transformation, the arrows refer to heating and cooling (up and down, respectively) and $\Delta S^{\downarrow} = -\Delta S^{\uparrow}$ (if the heat capacity of the austenite and martensite is the same (i.e, $C_A \cong C_M$)).

2. Thermal hysteresis

Since the transformed volume fraction of the martensite, ξ, is proportional to the entropy of the martensite, the cooling branch of the $\xi(T^{\downarrow})$ curve can be calculated as the ratio of the partial and full area of the cooling DSC curve. It is given as (see Fig. 2.3 and Eq. 2.2) [10]:

$$\xi(T^{\downarrow}) = \frac{A_{Ms-T}}{A_{Ms-Mf}} = \frac{\int_{M_s}^{T} \frac{dQ^{\downarrow}}{T}}{\int_{M_s}^{M_f} \frac{dQ^{\downarrow}}{T}} \tag{2.2}$$

Similarly for the heating branch of the hysteresis. The dissipative energy can be calculated from the area of the hysteresis, and the elastic energy contribution is related to the slope of the ξ-T curve (see also Fig. 1.5 in section 1.1.2).

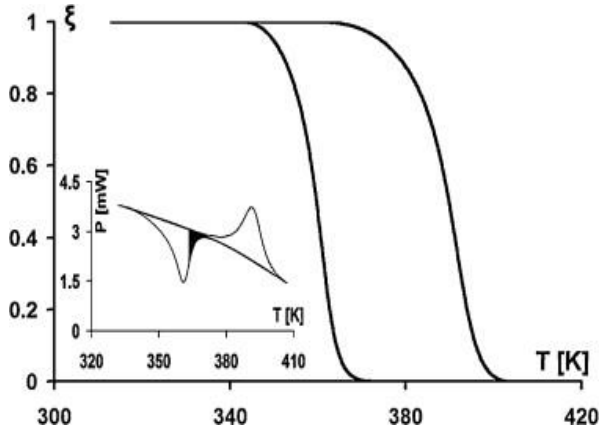

Figure 2.3 Hysteresis loop, $\xi(T)$, obtained from the DSC curves (shown in the insert) [10].

DSC curves were measured during heating and cooling for $Ni_{45}Co_5Mn_{36.6}In_{13.4}$ single crystal at different rates (10, 1, and 0.3 K/min). A driving rate of 0.3 K/min was used for the splitting of the peaks on the DSC curves. The masses of the specimens were 13 mg and 35 mg.

I also measured the DSC curves, with 10 K/min heating/cooling rate for the three different $Ni_{51}Fe_{18}Ga_{27}Co_4$ single crystals. The masses of the quenched and austenite-stabilized samples were 385 mg, while it was 18 mg for the SIM-aged specimen.

2.2.2 Simultaneous AE and DSC

Simultaneous AE and DSC measurements were performed in our DSC device (with a homemade accessory) with the help of a Sensophone AED-404 Acoustic Emission Diagnostic Equipment (developed and manufactured by Geréb and Co., Ltd., Budapest, Hungary). The signals are received, filtered, and processed by AED-404, and then it transmits the measurement to the control computer via a USB cable (see Fig. 2.4).

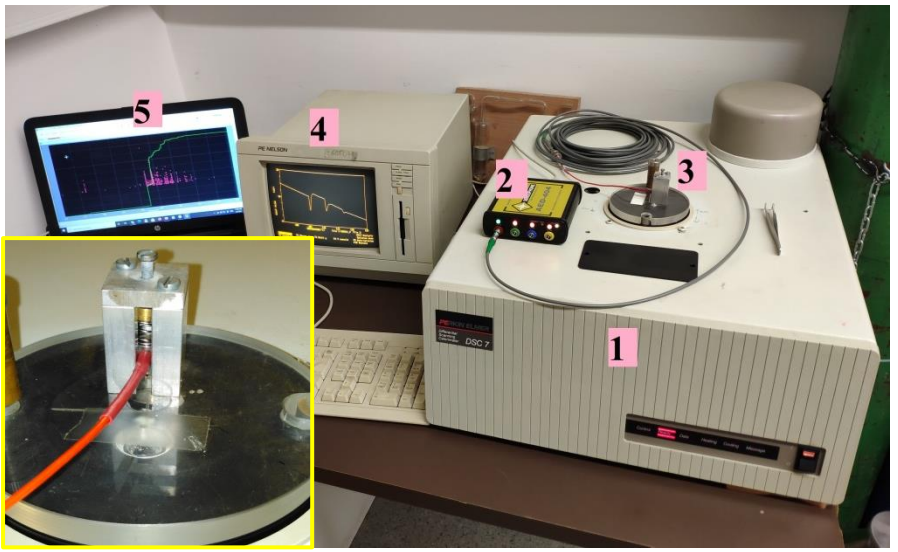

Figure 2.4 Simultaneous DSC and AE setup, **1:** DSC, **2:** Sensophone AED-404, **3:** Piezoelectric sensor coupled to the sample surface via steel waveguide, **4:** DSC controller and **5:** Control computer for AE. An insert (enlarged part 3) shows how the microphone is connected to the DSC.

For the detection of the acoustic signals, a piezoelectric microphone was used (MICRO-100s from Physical Acoustics Corporation, Princeton Junction, USA). A steel waveguide (of 15-mm long and 1-mm diameter) was used to couple the sensor to the sample surface. This waveguide protects the microphone from extremely variable temperatures and provides thermal isolation from the sample. The needle design was also necessary to minimize heat loss from the DSC sample holder. This waveguide was pressed onto the sample using a spring-loaded force-transmitting device (see an insert on Fig. 2.4) that transmitted the acoustic signals from the sample to the piezoelectric microphone.

The microphone has a good frequency response between 100 kHz and 1 MHz. The piezoelectric sensor produces a voltage (U_i) which is amplified with a 30 dB preamplifier and a main amplifier (logarithmic gain), with 90 dB dynamic range and band-pass operating frequency from 30 kHz to 1MHz, were connected directly to the microphone. A software band-pass filter used in the measurements was adapted to the frequency transmission of the main amplifier. In order to eliminate the high-frequency background noise components, a low pass filter was used. A high pass filter was applied for the elimination of the fluctuations of the baseline and possible DC components. The sampling rate of the analog-to-digital converter was 16 MHz.

Measurement in the martensitic state without heating/cooling (i.e. in the absence of phase transformation) was used to determine the threshold level. First, I set the threshold to the minimum and then increased until it reached the background noise level, and finally, I increased it by 3 dB for safety. The device automatically processes the signal of the microphones on the computer; only the most important parameters of each acoustic event are stored in the measurement files.

The simultaneous DSC and AE measurements were carried out for all three types of $Ni_{51}Fe_{18}Ga_{27}Co_4$ single crystals. The driving rate was 10 K/min (see the figures below in the next chapter).

2.2.3 Simultaneous AE and ME setup

Fig. 2.5 shows the experimental setup for the simultaneous measurement of AE and ME signals. The sample is in an aluminum sample holder, fixed on a copper cold finger cooled by liquid nitrogen. The temperature was changed with the help of a halogen lamp. The constant magnetic field was provided by placing the sample holder in the air-gap of a Weiss-type electromagnet. The temperature was measured by a copper-constantan thermocouple with a fixed ice-cold junction near to the sample. The temperature was controlled by a proportional-integral-derivative (PID) controller, which provides linear heating/cooling during the measurements.

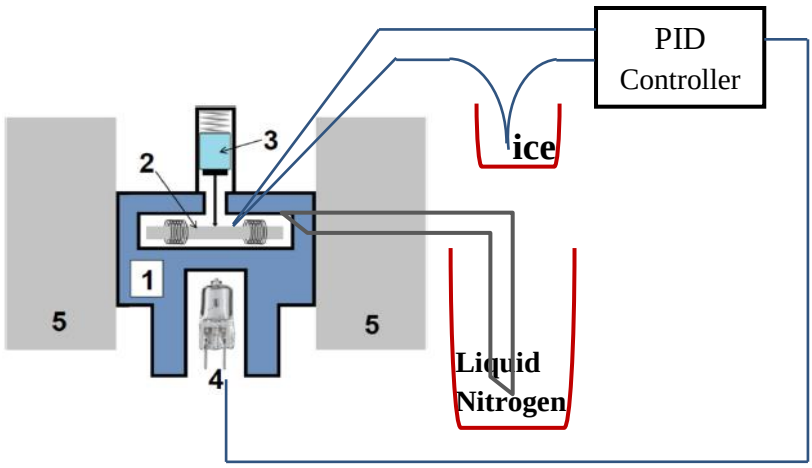

Figure 2.5 Experimental arrangement for simultaneous magnetic and acoustic emissions measurement; **1)** Al-block; **2)** sample with detector coils; **3)** AE sensor with steel waveguide; **4)** halogen lamp; **5)** magnet poles [46].

Two symmetrical copper detector coils (of 5 mm long and 0.05 mm diameter), wound around the sample (2×150 turns) with opposite winding directions to minimize the common-mode external noises, were used for the detection of magnetic signals. The signals of the detector coil were amplified with a homemade 60-dB gain grounded base amplifier. It has very good transmissibility in the 0-200 kHz frequency

range. For simultaneous detection of AE and ME signals, with a 5-MS/s/channel sampling rate, a National Instruments PCI-6111 multifunction data acquisition board in two-channel mode (instead of the Sensophone AED-404) was used. All parts of the setup were grounded in order to minimize the noises of the PID controller and the electromagnet. The simultaneous AE and ME measurements were carried out for $Ni_{45}Co_5Mn_{36.6}In_{13.4}$ single crystal without and with applying a constant external magnetic field in the range of 20-230 mT. The driving cooling/heating rates were 5 K/min (see the figures below in the next chapter).

2.2.4 Permeability

I used 1 kHz sinusoidal signals for the measurement of the magnetic permeability of the sample as the function of temperature. Two coils with turns n_1 and n_2 were placed around the sample and switched an alternating current (I_1) to the primary coil. The numbers of turns were $n_1 = n_2 = 200$. The magnetic field strength (H) is proportional to I_1, the number of turns n_1 and a constant K, depending on the sample geometry:

$$H = Kn_1I_1 = Kn_1I_{10}sin\omega t \tag{2.3}$$

In this arrangement, the amplitude of the voltage induced in the secondary coil (U_{20}) will be proportional to the permeability of the sample, a geometrical constant (containing the number of turns, cross section area of the sample etc.) as well as the amplitude and frequency of the current in the primary coil. By keeping the amplitude and frequency of the excitation current constant, the induced voltage depends only on constant factor (C) in addition to the permeability(μ):

$$B = \mu H \tag{2.4}$$

$$U_2 = -n_2\frac{d\Phi}{dt} = -n_2\frac{d(AB)}{dt} = -\mu\, An_2\frac{dH}{dt}$$

$$= -\mu\, n_2n_1AKI_{10}\omega cos\omega t \tag{2.5}$$

$$U_{20} = \mu\, n_2 n_1 AKI_{10}\omega = C\mu \qquad (2.6)$$

Here U_2 is the induced voltage in the secondary coil, Φ is the induction flux in the sample, B is the magnetic induction (flux density), A is the cross section area of the sample.

During the measurement, the y-scale is normalized with the permeability value measured at a reference temperature, which shows a relative (dimensionless) permeability value. Thus, the temperature dependence of permeability can be investigated without accurate knowledge of geometric factors that are otherwise difficult to determine. I placed the sample with a heating element into a stainless steel tube, filled in with He gas and immersed in liquid nitrogen. Using this arrangement, permeability measurements can be performed in the temperature range -190^{0}C-+200^{0}C.

2.2.5 Magnetization

Vibrating sample magnetometer was used to measure the magnetization curve of the austenite of the $Ni_{45}Co_5Mn_{36.6}In_{13.4}$ single crystal, parallel with the longitudinal axis of the sample (direction [011]).

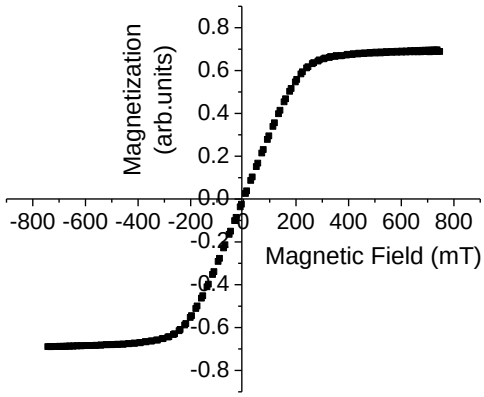

Figure 2.6 Magnetization of the austenite at room temperature. The hysteresis loop is very narrow and not visible.

2.3 Noises Statistical Analysis and the Critical Exponent

For the statistical analysis of the thermal, acoustic, and magnetic data recorded, I used a computer program written by my colleague (Dr. Tóth László Zoltán from our group), from which, I could plot the probability density functions and calculate the critical exponents for the avalanches.

The probability density functions for the different parameters (amplitude, energy, duration time, and size) of the avalanches were plotted as histograms on log-log plots by logarithmic boxing. In the logarithmic boxing, the entire scale was divided into sections of equal width on a logarithmic scale, and then counted how many avalanches are in each range. The logarithmic data binning was used, and due to the higher number of acoustic and magnetic events compared to the DSC measurements; the whole interval was split into 50 bins during the evaluation of the acoustic and magnetic emission and 15 bins for the thermal noises.

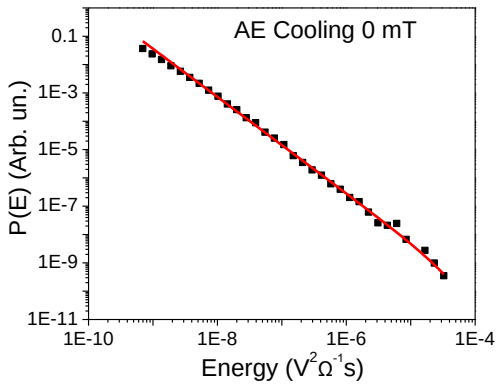

Figure 2.7 Energy probability density function for AE in $Ni_{45}Co_5Mn_{36.6}In_{13.4}$ single crystals in the absence of external magnetic field (with 5 K/min driving rate).

Due to the low signal level of the thermal noises in $Ni_{45}Co_5Mn_{36.6}In_{13.4}$ single crystal, 7 cycles were measured to get enough data for statistical analysis. The energy probability density

functions clear power-law behavior, as shown by Eq. (1.1). After logarithmic binning, usually I made a three parametric nonlinear fitting, using the Levenberg-Marquadt least-square method [50] (see, as an example, Fig. 2.7). At very low energy values, some points deviate from the power law, depending on the choice of the threshold value, so these points were not taken into account in the fitting.

For the estimation of the exponents, the maximum likelihood method (ML) [47] provides a more sophisticated way. The value of the exponent is given by:

$$\rho_x = 1 + k \left[\sum_{i=1}^{k} \ln \frac{X_i}{X_{min}} \right]^{-1}, \qquad (2.3)$$

where ρ_x is the exponent, X_i is the i^{th} data, X_{min} is the smallest data for which the evaluation is performed, and k is the multiplicity of the data set. This method is independent of the logarithmic binning, and the only free parameter is X_{min}. Plotting the obtained exponent as a function of X_{min} gives a curve on which, there is a plateau, i.e. a range within which the exponent becomes independent of X_{min} (See below Fig. 3.9 in the next chapter). Thus the average value of the plateau gives the correct exponent. It is worth mentioning that for less and less values of X_c, the ML estimation becomes less and less reliable [46].

Chapter 3

Results and Discussion

3.1 $Ni_{45}Co_5Mn_{36.6}In_{13.4}$ Single Crystal

3.1.1 Experimental Results

Fig. 3.1 shows the results of the DSC runs. The usual continuous envelope curves (at higher rates) split into small peaks at lower rates: see e.g. the curves belonging to cooling. It can also be seen that the obtained separate peaks became smaller and difficult to separate them from the background. The peaks for heating, at 0.3 K/min driving rate, were already almost at the level of background (and are not shown in this figure).

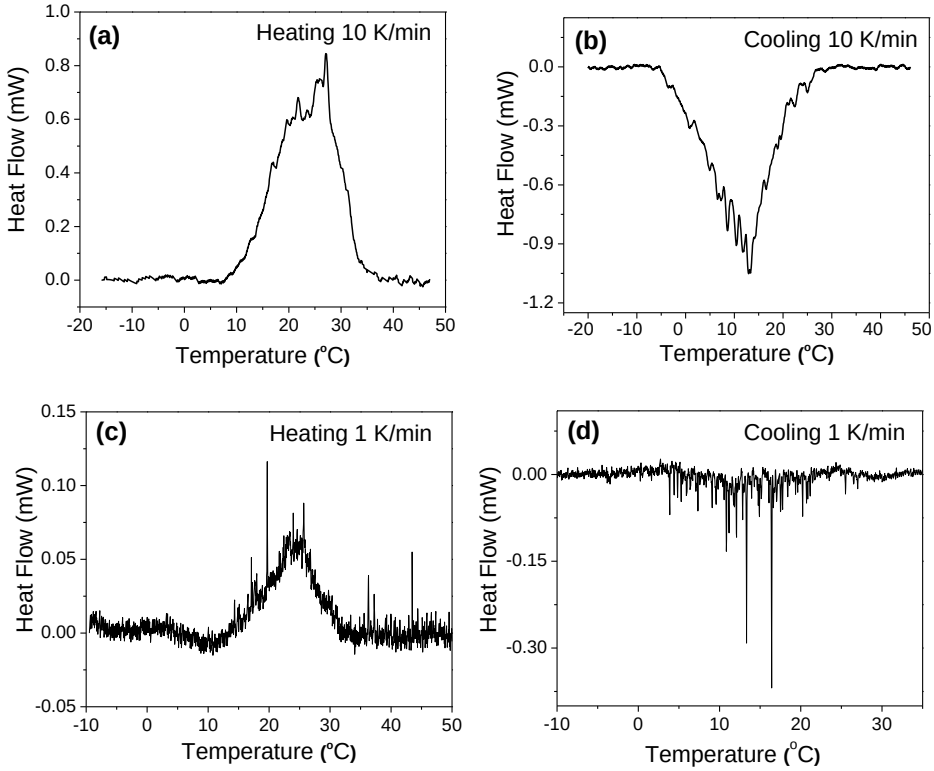

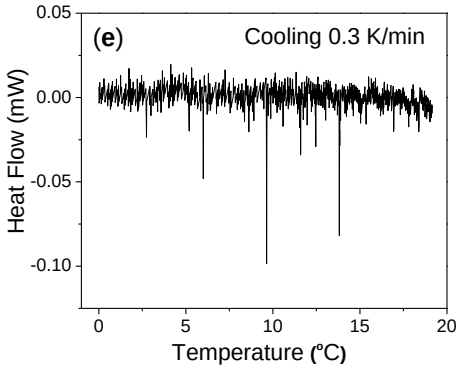

Figure 3.1 DSC measurements for heating (a, c) and cooling (b, d, e) for the $Ni_{45}Co_5Mn_{36.6}In_{13.4}$ single crystals (at 10 (a, b), 1 (c, d), and 0.3 K/min (e) driving rates).

Since the permeability of the austenite is much higher than of the martensite, there is an abrupt change in the permeability of the samples and the hysteresis loop could be determined (Fig. 3.2a). The hysteresis loop was also constructed from the DSC curves (Fig. 3.2b) and it is in good agreement with Fig. 3.2a. The transformation entropy was about 20 J/kg.K.

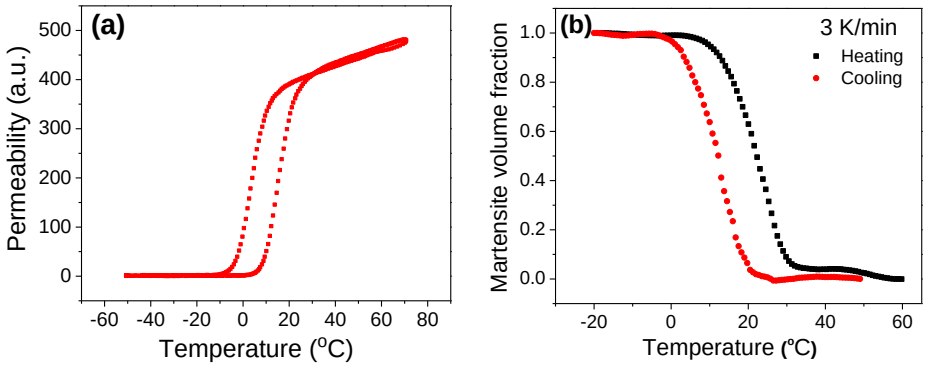

Figure 3.2 Hysteresis loops (a) from the permeability measurement at 5 K/min (parallel with the [011] direction) and (b) from the DSC curves at 3 K/min.

The overlaps of the peaks of the DSC curves below 1 K/min were more moderate and the real areas of the peaks could be estimated. Thus, the energy distribution, constructed from the corrected peaks belonging to 0.3 K/min showed indeed a power law behavior with a cutoff region (Fig. 3.3a). Fig. 3.3b shows the maximum likelihood fitting, illustrating that the relatively high value of the cutoff influences the energy exponent: we can compare this curve to the curve displayed in Fig. 4b of [51] for the cutoff $\Lambda=E_c=10$. Since there is no expressed plateau on Fig. 3.3b, the value of ε can be considered as an asymptotic value, and the error is relatively large: (about ±0.3, taking also into account the narrow energy interval, the reproducibility, and the sensitivity to the rate of cooling and the choice of the threshold).

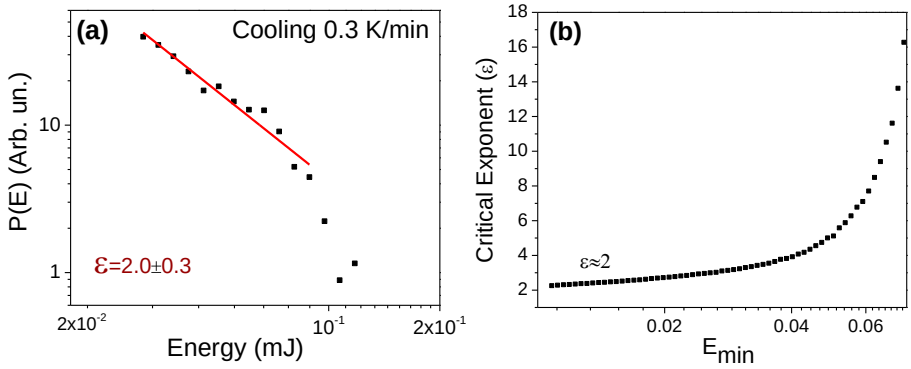

Figure 3.3 (a) Energy density function for cooling with 0.3 K/min (see Eq. (1.10)) (7 heating/cooling cycles, the number of hits was 3600). The unit of energies is mJ (estimated from the DSC values in mW and taking t=1s). The slope of the straight line fitted to the linear part of the curve gives ε=2.0 ±0.3. (b) Maximum likelihood fit; the asymptotic value is about $\varepsilon\cong 2$.

I used a new sample for the simultaneous AE and ME measurements and preliminary temperature runs indicated that the transformation temperatures were different from those of the previous samples, which can be probably related to the thermal history of the sample and the potential differences in the composition.

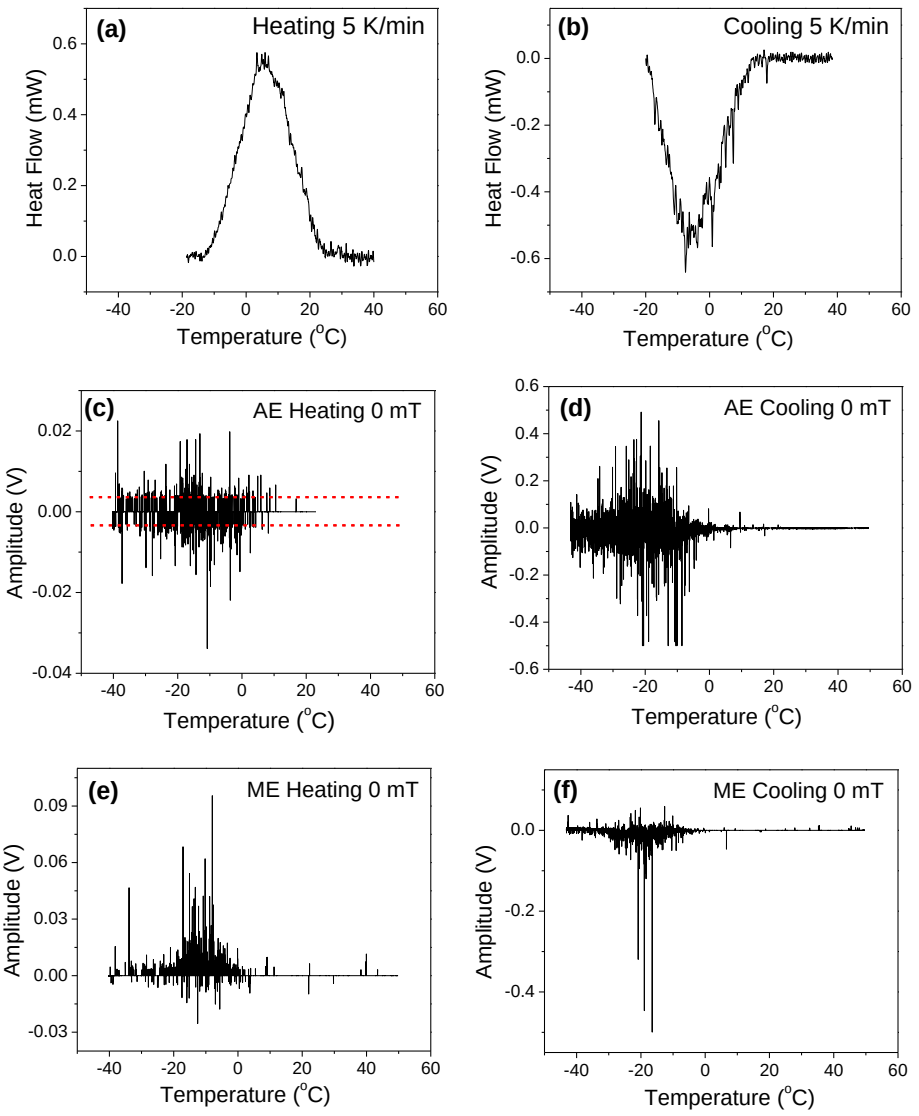

Figure 3.4 Results for heating and cooling of the $Ni_{45}Co_5Mn_{36.6}In_{13.4}$ single crystals at rate 5 K/min: DSC (a, b), acoustic emission (c, d), and magnetic emissions (e, f) signals, respectively. The horizontal dotted lines in (c) indicate the threshold level.

The mass of the new sample was 35 mg. The results of the DSC runs, acoustic (AE), and magnetic emissions (ME) signals (at 5 K/min rates) are displayed in Fig. 3.4. Since the AE activity was very low

during heating (Fig. 3.4c), the A_s and A_f temperatures can not be determined obviously. Energy probability density functions belonging to B=0 during heating and cooling are shown in Fig. 3.5.

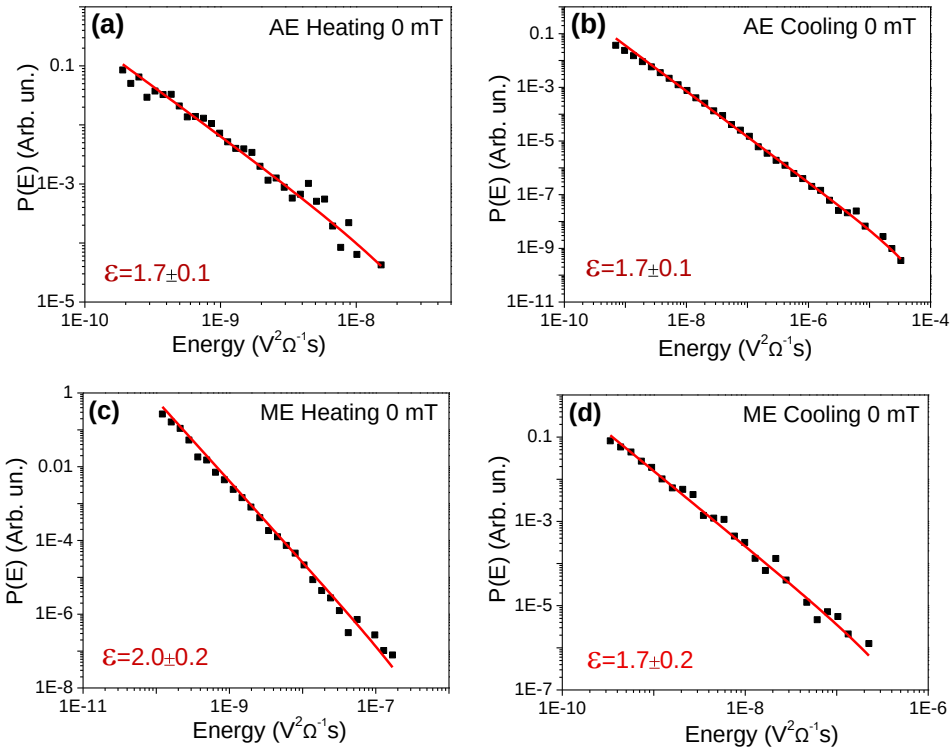

Figure 3.5 Energy probability density functions obtained from AE and ME measurements of $Ni_{45}Co_5Mn_{36.6}In_{13.4}$ single crystals at 5 K/min and B=0. The numbers of hits were 414 for a), 30063 for b), 12212 for c) and 1097 for d), respectively.

The values of the critical energy exponent for AE were the same for heating and cooling (ε=1.7 ± 0.1), in agreement with the exponent from DSC within the experimental error. This also confirms the general rule [40]: both methods (DSC and AE) provide the energies of the individual events, and thus the energy exponents should be the same. The signal-to-noise ratio of the acoustic and magnetic noises was poor at B=0 mT (e.g. Fig. 3.4c). Thus, simultaneous AE and ME

measurements in the presence of constant external magnetic fields (between B=20-230 mT), parallel with the longitudinal axis of the sample (direction [011]), were also performed (Figs. 3.6-3.8).

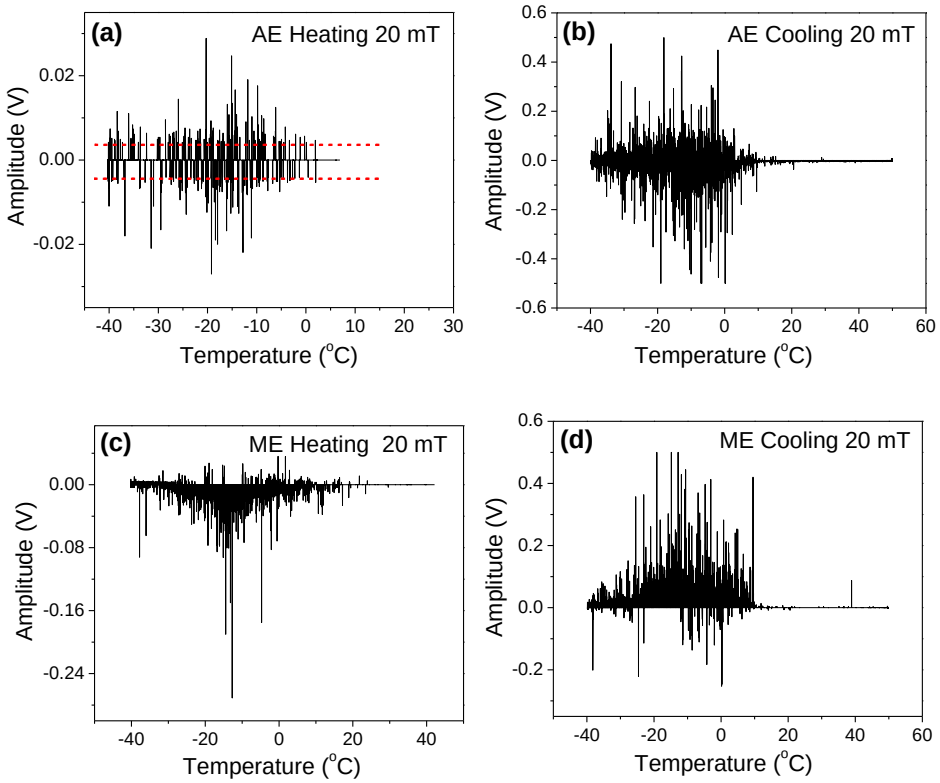

Figure 3.6 AE (a, b) and ME (c, d) signals for heating and cooling at constant B=20 mT for $Ni_{45}Co_5Mn_{36.6}In_{13.4}$ single crystals.

It can be observed that, at B=0 mT, the peaks are small (see the scale on the vertical axis of Fig. 3.4) and the whole spectrum is very noisy. The magnetic peaks are higher at B=20 mT (Fig. 3.6) and have characteristics similar to magnetic noises measured during martensitic transformations [52]. It can also be seen that the peaks of ME signals for heating and cooling are mainly bidirectional at B=0 mT (i.e. there are positive and negative signals), while they become more and more unidirectional with increasing the external field (see the results at B= 20, 30, and 230 mT).

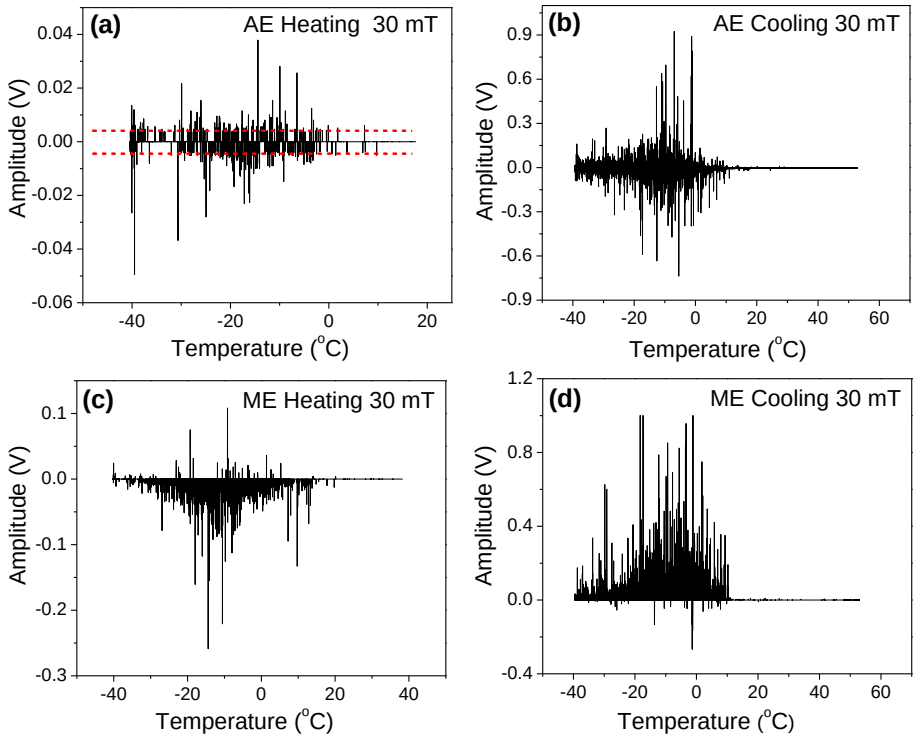

Figure 3.7 AE (a, b) and ME (c, d) signals during heating and cooling at constant B=30 mT for $Ni_{45}Co_5Mn_{36.6}In_{13.4}$ single crystals.

From the comparison of ME at B=0 mT and B=230 mT (Figs. 3.4f and 3.8d), one can also see that the magnetic activity inceases. Nevertheless, the critical power law exponents both for ME and AE signals were independent of the external magnetic field, within the experimental errors (Tables 3.1 and 3.2).

Table 3.1 The critical exponents for AE at different external magnetic fields at 5 K/min. The error bars are $\Delta\varepsilon=\pm0.1$ and $\Delta\alpha=\pm0.3$).

Critical Exponent		**0 mT**	**20 mT**	**30 mT**	**230 mT**
Energy, ε	up	1.7	1.8	1.8	1.7
	down	1.7	1.7	1.7	1.7
Amplitude, α	up	2.9	2.4	2.6	2.7
	down	2.4	2.4	2.4	2.6

Table 3.2 The critical exponents for ME at different external magnetic fields, at 5 K/min driving rate. The error bars are typically ±0.1 and it was ±0.2 for the values at B=0mT)

Critical Exponent		0 mT	20 mT	30 mT	230 mT
Energy	up	2.0	1.8	1.6	1.6
	down	1.7	1.7	1.6	1.7
Amplitude	up	2.1	2.4	2.4	2.1
	down	2.3	2.3	2.2	2.2
Area	up	2.3	2.3	2.2	2.2
	down	2.2	1.9	1.9	2.2
Width	up	2.3	2.4	2.5	2.5
	down	2.5	2.2	2.2	2.5

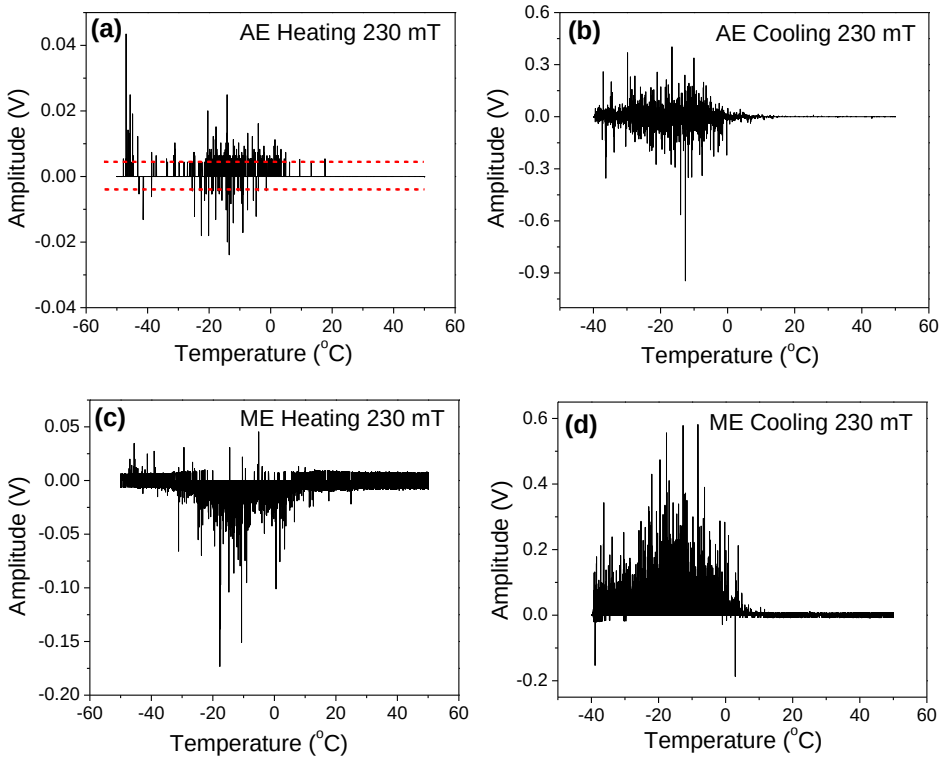

Figure 3.8 AE (a, b) and ME (c, d) during heating and cooling at *B*=230 mT for $Ni_{45}Co_5Mn_{36.6}In_{13.4}$ single crystals.

The maximum likelihood fit for the P(E) function of AE during cooling in B=30 mT is shown in Fig. 3.9. We can see that there is an expressed plateau and there is no kink on this curve. The latter fact indicates there is no overlap of different elementary processes, in accordance with Figs. 2b and 3b of [51]: a kink appeared on the maximum likelihood curve, due to the overlap of two distinct processes with different exponents.

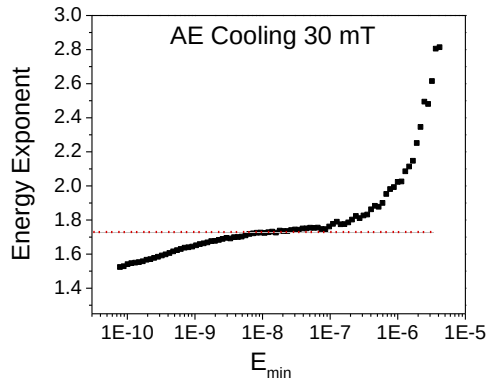

Figure 3.9 Estimation of the AE energy exponent by the maximum likelihood method (cooling in B=30 mT; see also Fig. 3.7b).

It was observed in Ref. [53] that in a polycrystalline alloy, with almost the same composition like ours, the forward A/M transformation was isothermal, while the reverse one was athermal. Thus, the following additional measurement has been carried out. We, before the M_f would be reached, stopped the cooling at -34 ^oC and kept the temperature constant for 5 min. Then, we continued the cooling down up to -60 ^oC. Fig. 3.10 shows the AE and ME noises versus the time at B=30 mT. It can be seen that there was no AE and ME signals during dwelling, but we can see a well visible activity appears with continued cooling. Similar results were obtained at B=0 mT. The energy probability density functions, determined separately before and after dwelling (part 1 and part 2, respectively), are shown in Fig. 3.11. The energy exponents for both AE and ME were the same in both parts (ε=1.7 before and after with $\Delta\varepsilon$= ±0.1 for AE as well as ε=1.6 and ε=1.4 before and after, respectively, with $\Delta\varepsilon$= ±0.2 for ME).

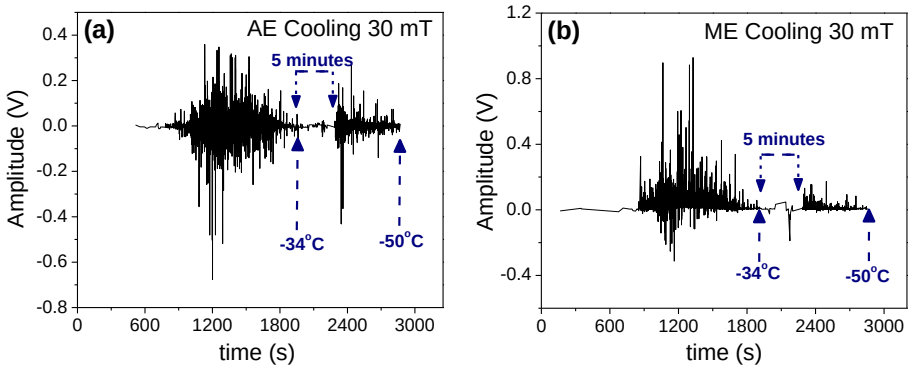

Figure 3.10 AE and ME during cooling in B=30 mT in $Ni_{45}Co_5Mn_{36.6}In_{13.4}$ single crystals (at 5 K/min rate).

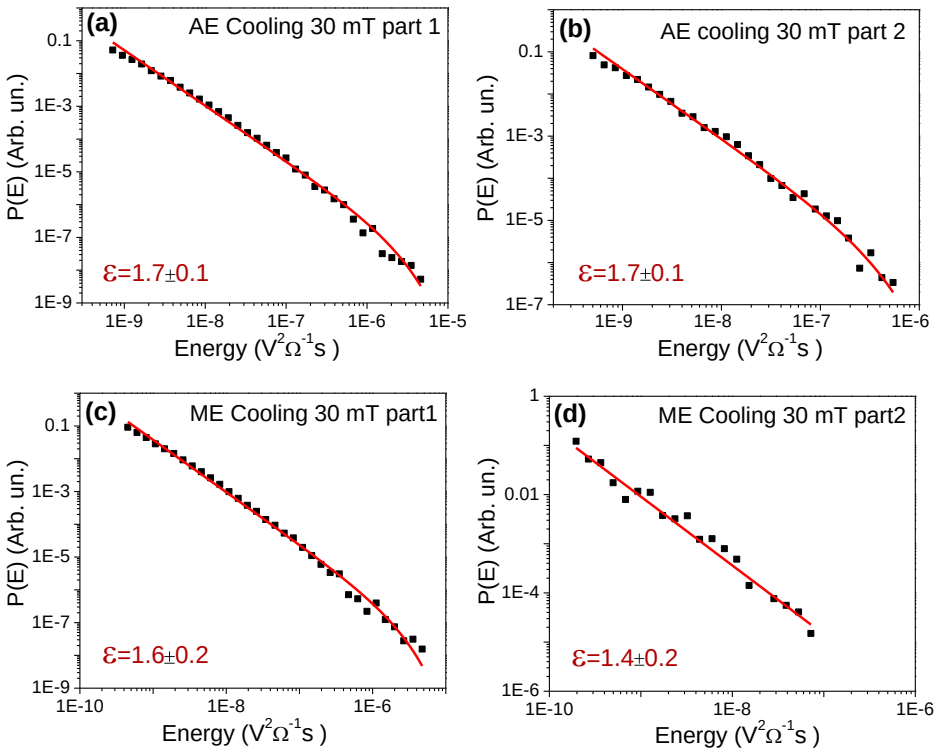

Figure 3.11 Energy probability density functions from AE and ME measurements, during cooling in $Ni_{45}Co_5Mn_{36.6}In_{13.4}$ single crystals at *B*=30 mT. The numbers of hits were 22187 for a), 2756 for b), 13683 for c) and 243 for d), respectively.

3.1.2 Discussion of the results

It was shown in [53] that in metamagnetic SMAs, the cooling transformation was usually isothermal, while the heating one showed athermal character. Usually, such behaviour was not observed in conventional ferromagnetic SMAs, like the NiMnCoIn alloys studied here. In addition, it was obtained that the exponents for cooling and heating were different in a wide range of shape memory alloys (i.e an asymmetry was observed) [32], [37], [39], [46], [52]. Thus it is worth to compare e.g. the energy exponents obtained from our experiments: Table 3.3 contains the results for ε, obtained at B=0mT in ferromagnetic SMAs investigated so far, including the present metamagnetic SMA.

Table 3.3 Energy exponents, ε, for heating (up) and cooling (down) from thermal DSC, AE, and ME noises in Ni_2MnGa, $Ni_{19}Fe_{18}Ga_{27}Co_6$ and $Ni_{45}Co_5Mn_{36.6}In_{13.4}$ single crystalline FMSMAs.

Ni_2MnGa [39], [46] (austenite: cubic martensite: monoclinic)					
DSC		AE		ME	
up	down	Up	down	up	down
-	1.7 ± 0.2	1.68±0.04	1.56±0.04	1.95±0.03	1.57± 0.03
$Ni_{49}Fe_{18}Ga_{27}Co_6$ [32], [37], [52] (austenite: $L2_1$, cubic martensite: $L1_o$, tetragonal, or 10M/14M modulated monoclinic + $L1_o$)					
DSC		AE		ME	
up	down	up	down	up	down
-	2.0± 0.1	1.7 ± 0.1	2.0 ± 0.1	1.6± 0.1	1.7± 0.1
$Ni_{45}Co_5Mn_{36.6}In_{13.4}$ (austenite: B2 or $L2_1$, cubic martensite: $L1_o$, tetragonal, or 10M/14M modulated monoclinic or 10M/14M modulated monoclinic + $L1_o$)					
DSC		AE		ME	
up	down	up	down	up	down
-	2.0± 0.3	1.70± 0.1	1.70± 0.1	2.0± 0.2	1.7± 0.2

The results in Table 3.3 show that while the asymmetry is positive for Ni_2MnGa (the exponents are larger for heating than that for cooling), there is a slight negative asymmetry for $Ni_{49}Fe_{18}Ga_{27}Co_6$ and it is practically zero for the present $Ni_{45}Co_5Mn_{36.6}In_{13.4}$ metamagnetic SMA. In addition, the energy exponents of different noises are almost the same within the error bars for the same direction in the three alloys, which indicate that all types of noises originate from the intermittent displacements of the propagating interfaces during martensitic transformation.

The asymmetry of the energy exponents is zero in our metamagnetic SMA, although the noise activities were a bit larger for cooling, which would belong to a positive asymmetry [38]. Thus we could not detect this small effect in the exponents within the present error bars. We practically could not detect AE and ME noise activities during dwelling. The same values of the exponents before and after dwelling showed that the character of the martensite growth process is the same. Thus, we confirmed the power law behavior in both stages and thus the stationary of the energy probability density functions (see also e.g. Ref. [54]). The zero noise activity during dwelling can be explained only if:

i) The dwell time (5 min) was too short: in Ref. [53] the martensite volume fraction changed from 8% up to 13% during 30 min,
ii) If there is any growth process during dwelling, then it should be different and much less noisy,
iii) The cooling process is athermal.

The asymmetry can also be different in polycrystalline and single crystalline samples (see e.g. Ref. [55]). Thus, our result suggests that the cooling process is also athermal in our single crystal. We have to discuss the following effects of the external magnetic field on the ME signals: i) the magnetic field increased the magnetic noise activity, ii) with increasing the external field, the polarity of the ME signals increased. In our material, all dominant changes of magnetization

should be caused by the change of the volume fraction of the austenite (the martensite is weakly magnetic and the austenite is ferromagnetic [56]–[58]). This, during cooling at B=0 mT, leads to bipolar magnetic signals (Fig. 3.12a) due to the randomly oriented domains in the austenite (see also Fig. 2.6 in the previous chapter).

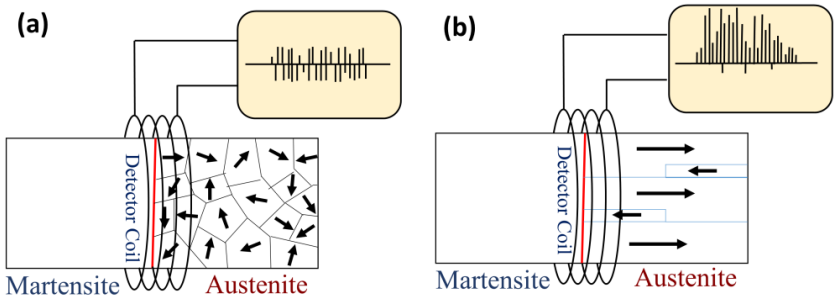

Figure 3.12 Effect of the magnetic field on the polarity of the magnetic signals: more ordered and unidirectional magnetic domains appear with increasing the field.

Since the external magnetic field (230 mT) is large enough to almost magnetically saturate the austenite, the intermittent jumps of the interface result in unipolar signals (see Fig. 3.12b and the experimental results in Fig. 3.8d). Furthermore, the amplitudes of the signals should be larger in a saturation field; since the magnetization jumps will be larger (the flopping magnetization has the same orientation). A similar explanation holds for heating.

In our sample, the AE and ME exponents are independent of the external magnetic field, while in ferromagnetic Ni_2MnGa single crystal the exponents of the AE amplitude and energy depend on the magnetic field and the asymmetry between heating and cooling disappears gradually by increasing the field [46].

3.2 $Ni_{51}Fe_{18}Ga_{27}Co_4$ Single Crystal

3.2.1. Experimental Results

Figs. 3.13 and 3.14 show the DSC results for heating and cooling of the quenched and SIM-aged samples, respectively.

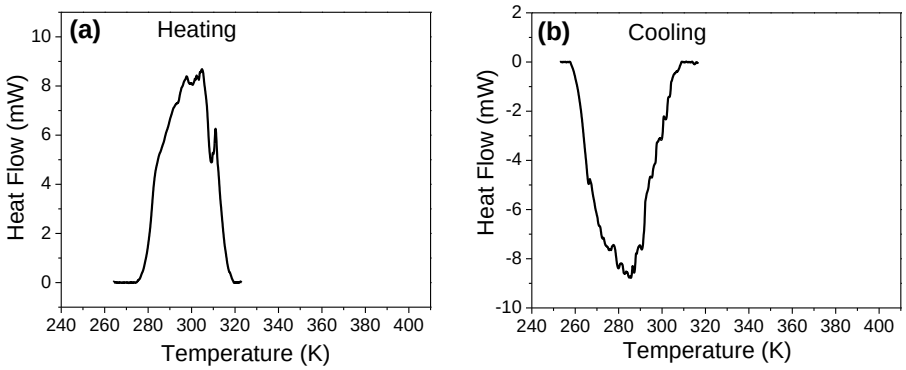

Figure 3.13 DSC results during heating (**a**) and cooling (**b**) for the quenched $Ni_{51}Fe_{18}Ga_{27}Co_4$ single crystals.

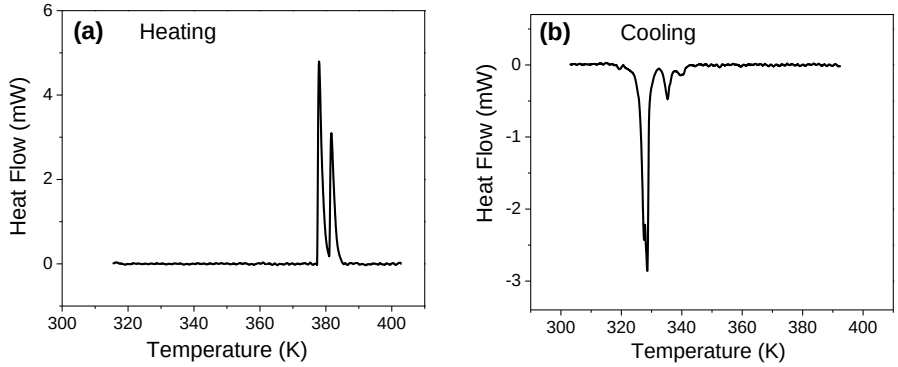

Figure 3.14 DSC runs during heating (**a**) and cooling (**b**) of the SIM-aged $Ni_{51}Fe_{18}Ga_{27}Co_4$ single crystals.

Since in the SIM-aged sample the burst-like transformation was accompanied with a large, sudden shape change [8], I fixed the sample into the sample holder of the DSC by using silicon grease. It is why the mass of the SIM-aged sample was about twenty times smaller: this

made it easier to fix the sample. In addition, due to the very large changes of local stresses during transformation, the sample was broken into small pieces during heating/cooling. No cracking was observed in the smaller samples even after many cycles, and thus all measurements were carried out on the same piece of sample. It was shown in [46] that decreasing sample' size resulted only in a split of the DSC peaks, but, e.g., the AE energy exponents did not change. Thus it can be supposed that the smaller size did not cause disturbing size effects. I also checked this by carrying out AE measurements on another piece of the broken sample (with three times larger mass) and the same characteristic features were obtained.

It can be seen from the DSC hysteresis loops (see Figs. 3.13–3.15 and Table 3.4) that in the SIM-aged sample the transformation temperatures were shifted to higher temperatures and the transitions were sharper. Also, the DSC curve split into separate peaks, for the SIM-aged sample, clarifying a stepwise character of the transformation.

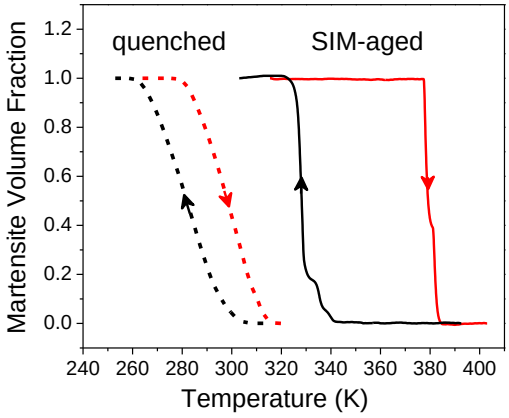

Figure 3.15 DSC hysteresis loops for the quenched and SIM-aged $Ni_{51}Fe_{18}Ga_{27}Co_4$ single crystals at 10 K/min driving rate.

The start and finish temperatures, obtained from the DSC and AE data, are in good agreement with each other (Table 3.4). The higher sensitivity of the AE method as compared to the DSC can explain the observed acoustic activity above the M_s temperature (obtained from the

DSC: Table 3.4) during cooling for the SIM-aged sample (Figs. 3.14b and 3.16d). Austenite stabilization heat treatment had no detectable effect. The values of the transformation entropy (Table 3.5) show that it did not change after austenite stabilization heat treatment, while it decreased by about 36% for the SIM-aged sample.

Table 3.4 Transformation temperatures for the three different $Ni_{51}Fe_{18}Ga_{27}Co_4$ single crystals, as obtained from DSC and AE measurements. The error bars are about ±3 K.

Type of Sample	A_S	A_f	M_s	M_f
AE for Quenched	270	337	317	254
DSC for Quenched	276	320	308	259
AE for Austenite Stabilized	270	337	317	254
DSC for SIM-aged	377	386	343	317

Table 3.5 Averaged values of the transformation entropy, -Δs, calculated from the heating and cooling DSC curves, for the three different $Ni_{51}Fe_{18}Ga_{27}Co_4$ single crystals (Δs=±0.08 J/mol.K, within which, the values for heating and cooling are also the same).

−ΔS	Quenched	Austenite Stabilized	SIM-aged
(J/mol·K)	0.94	0.94	0.60

Fig. 3.16 shows the measured acoustic signals for the quenched and SIM-aged samples at 10 K/min rate (plots for the austenite stabilized samples are not shown because they are similar to those of the quenched sample). As the mass of the quenched sample is about 20 times larger, the number of AE events for the quenched sample is much higher than for the SIM-aged one (see also the numbers of hits, *N*, the sum of the AE peak energies, and the average peak energies in Table 3.6).

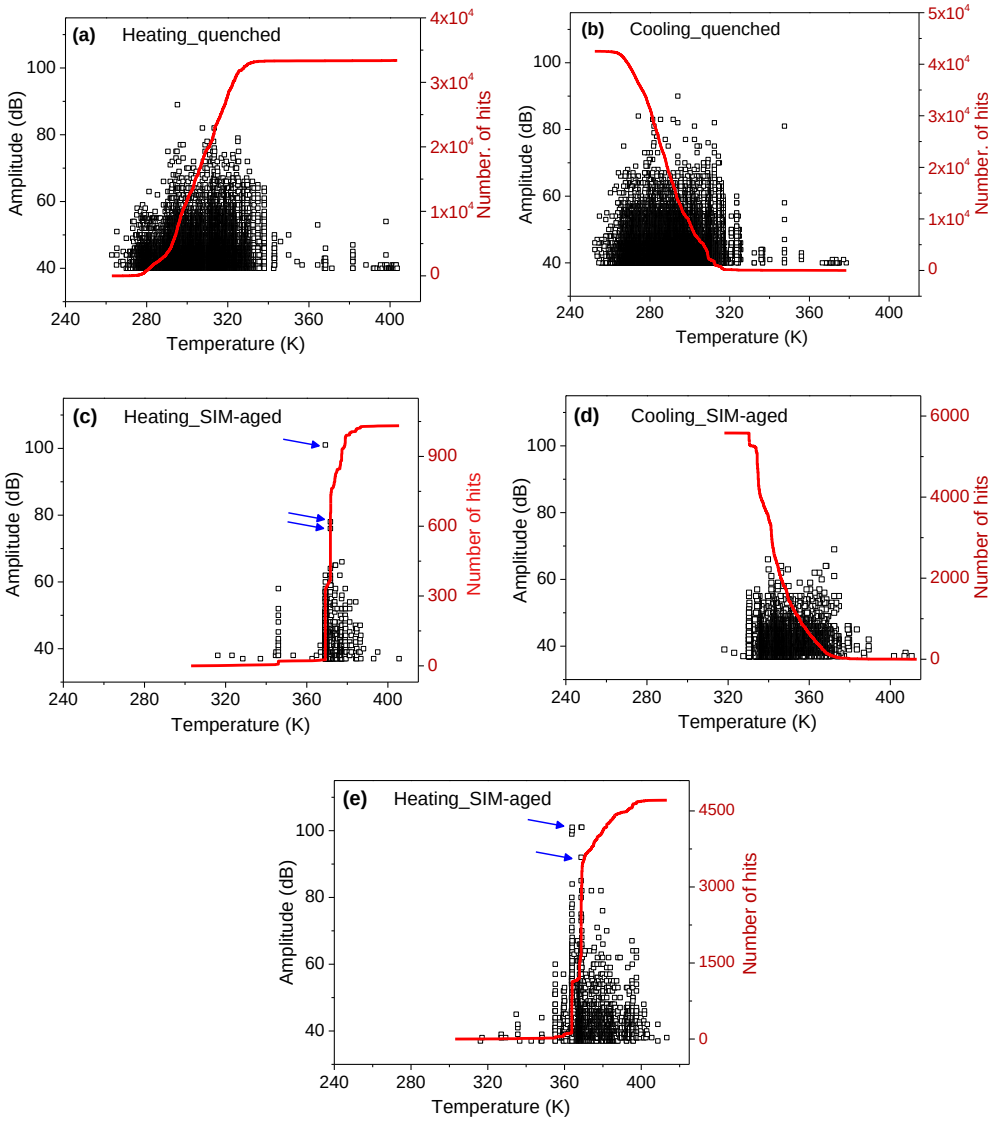

Figure 3.16 AE signals: quenched (**a**,**b**), and SIM-aged (**c**,**d**) $Ni_{51}Fe_{18}Ga_{27}Co_4$ single crystals. (Each point belongs to an acoustic emission (AE) event, and the cumulative number of them is indicated by the continuous red line for the transition). The three points in Fig. 3.16**c**, (see arrows), are the solitary high energy hits for *m=18 mg* (see also Fig. 3.19a), whereas Fig. 3.16e displays the same plot for the SIM-aged sample with *m=47 mg*.

Table 3.6 AE critical energy exponents, ε and energies of hits for the three different $Ni_{51}Fe_{18}Ga_{27}Co_4$ single crystals at 10 K/min. E_t and E_{av} are the sum of peak energies ($\sum_i E_i$), as well as the average peak energy ($E_{av} = {\sum_i E_i}/{N}$). The energies are given in $\mu \cdot V^2 \cdot \Omega^{-1}$s units.

	Quenched	Austenite Stabilized	SIM-aged	SIM-aged, removing high energy events
AE for Heating				
N	32077	18891	967	964
E_t	6.1×10^4	9.2×10^3	1.9×10^6	769
E_{av}	1.9	0.5	1970	0.8
ε	1.84±0.06	1.97±0.06	-	1.7±0.3
AE for Cooling				
N	40500	26930	5278	-
E_t	1.4×10^5	4.0×10^4	1062	-
E_{av}	3.6	1.5	0.2	-
ε	1.87±0.06	1.94±0.12	2.0±0.1	-

Figs. 3.17–3.19 shows the *P(E)* functions for the three different types of samples. These functions show linear behaviour over three to four orders of magnitude, i.e., we can take that $exp(-E/E_c) \cong 1$ in Eq. (1.10), indicating the number of high energy hits became very low before the cut-off effect would be visible. Table 3.6 includes the values of the critical energy exponents.

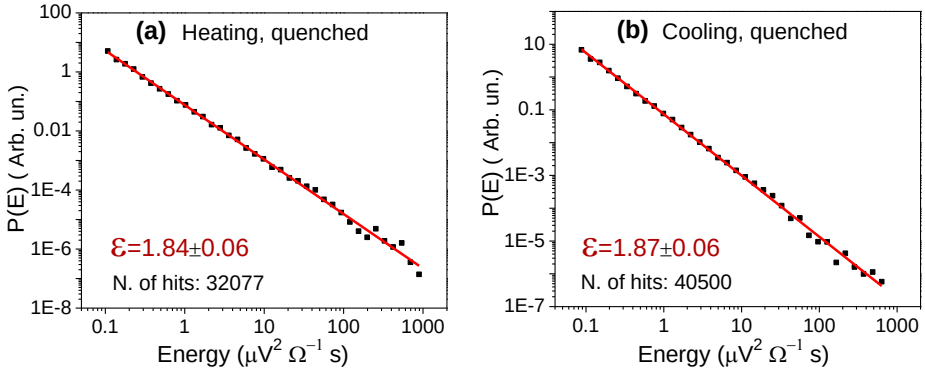

Figure 3.17 Energy probability density functions obtained from acoustic emission measurements during heating (**a**) and cooling (**b**) in quenched $Ni_{51}Fe_{18}Ga_{27}Co_4$ single crystal.

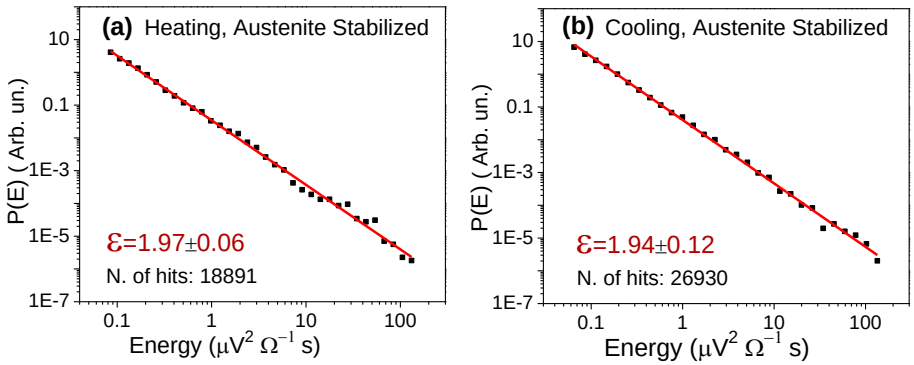

Figure 3.18 Energy probability density functions obtained from acoustic emission measurements during heating (**a**) and cooling (**b**) in austenite stabilized $Ni_{51}Fe_{18}Ga_{27}Co_4$ single crystal.

The critical exponents for the SIM-aged and quenched samples are the same within the error bars (Table 3.6). At the same time, for heating in the SIM-aged sample there are high energy solitary AE hits on the P(E) function, which do not fit to the straight line drawn to the remaining part of the plot in Fig. 3.19a. I checked the appearance of such AE hits by carrying out eight runs and I got similar results in all runs. In addition, they appeared at the same temperature (see the marked points in Fig. 3.16c). Besides, the average peak energy, E_{av},

after removing the last three high energy points, is in the same order of magnitude as the values for the other three cases in Table 3.6.

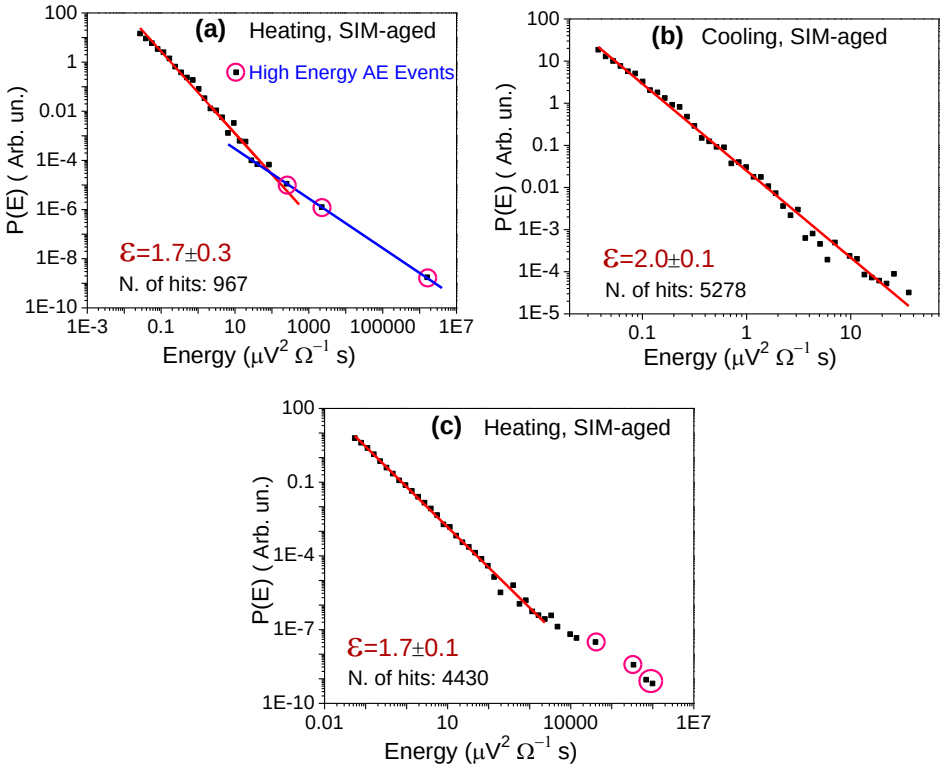

Figure 3.19 AE *P(E)* functions for heating (**a**) and cooling (**b**) for the SIM-aged $Ni_{51}Fe_{18}Ga_{27}Co_4$ single crystals with *m=18mg*. For comparison, (**c**) displays the distribution for heating with *m=47mg* mass: the slopes of the lines, fitted to the first parts, are the same in (**a**) and (**c**).

3.2.2 Discussion of the results

Our hysteresis loops can be compared to the results published in [7], where the temperature dependence of the transformation strain (ε_{tr}~T plots), the start and finish temperatures (measured also by DSC) were published on the same single crystal, with the same heat treatments. The schematic hysteresis loops, the shift and the increase of

the width of the hysteresis obtained from the data of [7] are shown in Fig. 3.20. One can conclude that the agreement with Fig. 3.15 is reasonable.

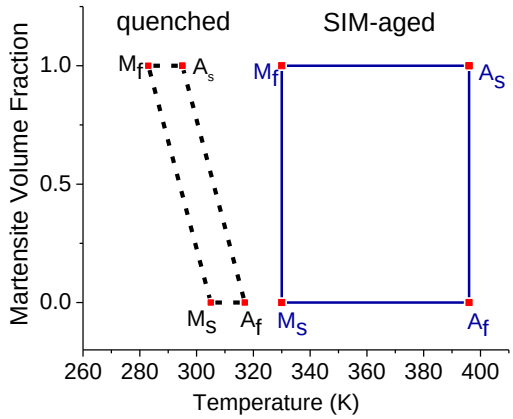

Figure 3.20 Schematic hysteresis loops from [7].

The value of the transformation entropy, calculated from our DSC results, can be compared with the value estimated from the Clausius–Clapeyron relation [10]:

$$\frac{\partial \sigma_{cr}}{\partial T} = -\propto \frac{\Delta s}{\varepsilon_{tr}} \tag{3.1}$$

(ε_{tr} is the transformation strain and $\propto$ is the reciprocal value of the molar volume, V_M; $\propto = 1/V_M$). The temperature dependence of σ_{cr} and ε_{tr} for the quenched sample are shown in Fig. 3.21 (as calculated from the temperature dependence of σ versus ε_{tr} loops). It can be seen that the σ_{cr} versus T function (Fig. 3.21a) can be fitted with a straight line, of $\partial\sigma_{cr}/\partial T$ =3.27 MPa/K slope, between 350 and 550 K. Although there is a moderate temperature dependence of ε_{tr} (Fig. 3.21b), we can take the medium value of the transformation strain in the above interval in Eq. (3.1). Using the following values: $\partial\sigma_{cr}/\partial T$ =3.27 MPa/K, $\varepsilon_{tr} \cong$ 0.035, and V_M = 7.7x10^{-6} m^3/mole, one gets $\Delta s = -0.88$ J/mol·K, in a good agreement with the transformation entropy, shown in Table 3.5.

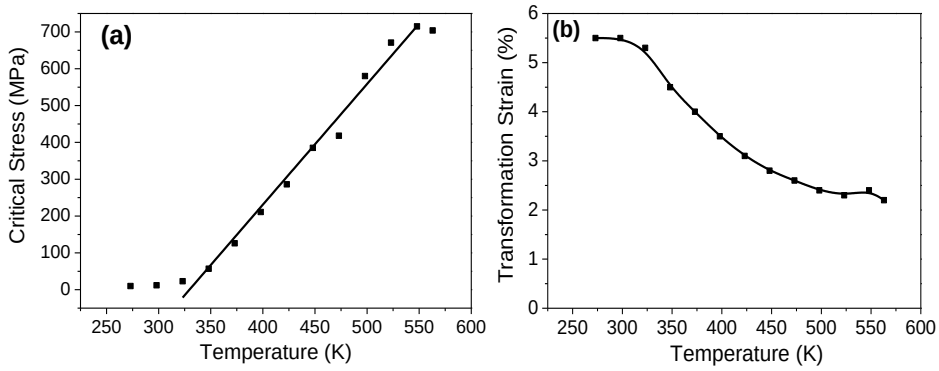

Figure 3.21 Temperature dependence of σ_{cr} (a) and ε_{tr} (b) for the quenched sample. In (a) the straight line shows where the linear fit can be applied.

We have shown in our recent paper [59], that the second derivatives of the elastic energy by the transformed martensite volume fraction are good measures of broadenings of the forward and reverse martensitic transformations (i.e. they are proportional to $\partial e^{\uparrow\downarrow}/\partial\xi$: see Fig. 1.5c). The SIM-aging caused an asymmetric change: the sharpening in $Ni_{53}Mn_{25}Ga_{22}$ and $Ni_{51}Fe_{18}Ga_{27}Co_4$ single crystals was stronger for heating than cooling. In addition it was obtained that, the thermoelastic balance condition was violated for the SIM-aged samples and the elastic energy contributions led also to a shift of the transformation temperatures, compensating the increase of T_o: $S_H = \Delta T_o + \frac{\Delta(E_t^{\uparrow} - E_t^{\downarrow})}{-2\Delta s}$, ($\Delta T_o$ is positive for martensite stabilized samples). It was also shown in [59] that the overall shift of the transformation, S_H in addition to shift of T_o, can also be dependent on the change of the elastic and dissipated energies ($\Delta E^{\uparrow\downarrow}$ and $\Delta D^{\uparrow\downarrow}$): due to the contributions of the elastic terms the dissipated energy per one cycle, ΔW_H, could decrease even if the area of the hysteresis has been increased: $\Delta W_H = \frac{\Delta D_t}{-\Delta s} + \frac{\Delta(E_t^{\uparrow} + E_t^{\downarrow})}{-\Delta s}$ (if the thermoelastic balance condition would be fulfilled $E_t^{\downarrow} = -E_t^{\uparrow}$ and the above correction would be zero).

The results of the AE measurements also provide some additional information on the effect of SIM-aging: see the results displayed in Figs. 3.17, 3.19, and Table 3.6. While the characteristic energy exponents are the same within the error bar, the following two striking features can be recognized:

i. There are high amplitude/energy events, falling above the points on the energy density function during heating.
ii. Disregarding these events, the average peak energy has a similar value to the others and the energy exponent agrees with the other three values (Table 3.6).

The solitary high amplitude/energy AE hits were observed for the sharper heating transition at one temperature. Fig. 3.16c indicates the high, almost vertical jump in the cumulative numbers at this temperature which corresponds to the position of the sharp peaks on the DSC curve (Fig. 3.14). Indeed, the envelope type DSC curves can be split into small individual peaks when one uses small investigated masses and/or appropriate low heating/cooling rates [40], [46], [60]. The large two peaks of DSC in Fig. 3.14a indicate sudden, high-velocity jumps corresponding to the transformation of a considerable amount of martensite volume fraction.

In general, the energies of the individual acoustic events and the energy dissipation during large jumps are related to each other [40], [41], [61], [62]. The amplitude of an acoustic emission signal is proportional to the velocity of the interface [41], [61], [62] (and E_i is proportional to ${U_i}^2$), the observed few large energy events should belong to jumps of high velocity. On the other hand, the fact that the characteristic exponents did not change after SIM-aging is a strong indication of the robustness of the power law behavior. The above results are similar to the effect observed in [63]: during twin boundary motion in Ni_2MnGa, the stress drops were accompanied with single dominant AE signals, while 98% of the AE signals were emitted during the intervals free of stress drops.

Our results on the austenite stabilization show that the change of the chemical order during the transformation from B2 to ordered $L2_1$ structure has no detectable effect (Table 3.6). There is one DSC result on this effect in the literature of ferromagnetic shape memory alloys: it was shown in $Ni_{53.5+x}Fe_{19.5-x}Ga_{27.0}$ (x =0, 0.5, and 1.5) alloys [64] that the transformation temperatures decreased with increasing $L2_1$ order, but no results on the transformation entropy were published.

Our ΔS results are in qualitative agreement with the results of [65], where about a 12% decrease for martensite stabilization and a minor increase (about 4%, which was close to the error bar) for the austenite stabilization was observed. Nevertheless, our results show that the change of ΔS cannot be simply related to the increase of the hysteresis width, since it alone would cause a much smaller effect. It is possible that magnetic contributions can also attribute the entropy change in ferromagnetic shape memory alloys [60], [64], [66], [67], and this calls for further investigations. Regarding the possible other contributions to ΔS, defects caused by the SIM-aging cannot be important. Indeed, in accordance with the arguments of [66]: "a homogeneous decrease of the chemical-free energy is the only effect of such stabilization"; the martensite stabilization results in a more ideal martensite microstructure (e.g., by annealing out of the frozen-in vacancies by quenching). In addition, according to [65], [68], [69] the change of the long-range order in the austenite has also a moderate effect.

The SIM-aged sample was broken into small pieces after few thermal cycles, most probably because of the large local stresses accompanied with the transformation. Thus, breaking results in stress relaxations of the SIM-aged samples. The presence of different twins means that large elastic energy can also be present in the quenched sample, (accumulated during cooling). But, since the dependence of the elastic constants usually has weak temperature dependence, the difference of the elastic energies of the A and M phases should provide a negligible contribution to the slopes of the free energies versus the temperature functions and thus should result in a negligible contribution to ΔS.

Summary

The basic aim of my PhD dissertation is to study the martensitic transformation in ferromagnetic shape memory alloys (SMAs), using noise measurement techniques. During the transformation, the motion of the interface between the austenite and martensite has a stop and go character, and we can detect different types of noises, such as thermal, acoustic, or magnetic emission. The statistical analysis of these noises can provide important information about the microscopic nature of the transformation. I have investigated the above noises in two different ferromagnetic SMAs, which are recently very promising in applications. The samples were prepared by our partners, in collaboration with Texas and Tomsk Universities in the United States and Russia, respectively.

A) $Ni_{45}Co_5Mn_{36.6}In_{13.4}$ Single Crystals:

It is a special kind of ferromagnetic SMAs, called meta-magnetic SMA, where there is a large difference between the saturation magnetizations of ferromagnetic austenite and weakly magnetic martensite phases. These alloys are very promising for actuators and magnetic refrigeration applications, based on the magnetocaloric effect. I was interested in studying the intermittent behavior of martensitic transformation, accompanied with a large change in magnetization, by detecting different noises in this alloy.

I measured the magnetic permeability curve and it was shown that there is an abrupt change in the permeability between austenite and martensite. From the measurement, I could also determine the transformation temperatures. I measured also the magnetization curve in the austenite phase at room temperature.

DSC curves were measured at different heating/cooling rates, and a low 0.3 K/min rate was enough for the splitting of the peaks (thermal noises). Because of the small number of events, I had to measure 7 cycles to reach a sufficient amount of data for the statistical analysis. The energy probability density function was clearly showing the power-law, and I determined the energy exponent with three-parametrical nonlinear fitting (least square method) and by maximum likelihood method, too. From the calorimetric measurements, I have constructed the hysteresis loop of the martensitic transformation (the martensite volume fraction as a function of temperature), and it was in good agreement with the permeability measurement. I measured acoustic and magnetic noises emitted during the transformation simultaneously at constant external magnetic fields (0-230 mT). The probability density functions for energy, amplitude, duration time, and size were plotted and showed the damped power law. The critical exponents were determined. It was obtained that:

A1) The energy exponents, calculated from the DSC, acoustic emission, and magnetic emission measurements, were the same within the experimental errors. This indicates that all the above noises originate from displacement discontinuities of the moving interfaces during martensitic transformation [P1, C1, C2].

A2) The exponents of the energy and amplitude distributions of the acoustic and magnetic signals were independent of the external magnetic field (between B=20 and 230 mT), indicating that the character of the martensitic transformation is independent of B at these values of magnetic field [P1, C1, C2].

A3) The magnetic noise packets contained voltage peaks in both (up and down) directions in a zero magnetic field. Application of a small external magnetic field (up to 230 mT), besides the increased activity of magnetic signals, caused a gradual change: the peaks became more and more unidirectional (during both heating and cooling) with increasing

field. This was explained by the increasing magnetization of the austenite [P1, C1, C2].

A4) The exponents during heating and cooling were the same in contrast to the expected asymmetry observed by our group in other ferromagnetic SMAs. This indicates that the main discontinuous events (energy dissipation as well as elastic energy accumulation/release), leading to noise emissions, should be the same in both directions [P1, C1, C2].

B) $Ni_{51}Fe_{18}Ga_{27}Co_4$ Single Crystals:

The stabilization of a certain martensite variant produced by uniaxial stress (stress-induced martensite stabilization; SIM-aging) is very important in applications. It extends the reversible two-way shape memory to higher temperatures and results in large superelastic deformation or rubber-like behavior (up to about 10-14%) in a martensitic state under the application of unidirectional stress or magnetic field. It was interesting to see how the stabilization of the martensite affects the characteristics of noises in both directions, and how it affects the entropy of the transformation. I have performed my measurements on three samples: Quenched, Austenite stabilized (I made heat treatment for the quenched sample at 573 K for 6h to stabilize the austenite), and SIM-aged (stabilize certain martensite variant by applying uniaxial stress) single crystalline $Ni_{51}Fe_{18}Ga_{27}Co_4$ samples. Simultaneous DSC and acoustic emission measurements were carried out with 10 K/min driving rate both for heating and cooling. The transformation temperatures were compared before and after SIM-aging. The thermal hysteresis was constructed, as well as the entropy of the transformation was calculated from the DSC curves for the samples. The statistical analysis for the acoustic activity was made to determine the energy exponent. Acoustic emission measurements provided interesting information about the details of the jerky character of the transformations and the effect of the SIM-aging. It was obtained that:

B1) Martensite stabilization by SIM-aging resulted in an expected shift of transformation temperatures to higher values, as well as the forward and reverse transitions became sharper, while the width of the hysteresis increased [P3, P4].

B2) There was no change in the acoustic energy exponents characterizing the power law behavior due to the SIM-aging effect [P3].

B3) Few high amplitude/energy solitary events appeared in the SIM-aged sample during heating, which were above the values corresponding to the extrapolated energy distribution curve, fitted at smaller energies. These high energy events were rationalized as high sudden jumps with large interface velocity during the phase transition. This velocity can be orders of magnitude larger than the other velocities with which the interfaces move in the not SIM-aged sample [P3].

B4) The transformation entropy was about 36% smaller after SIM-aging and was practically unchanged after austenite stabilization. These are in qualitative agreement with literature results in non-magnetic SMAs, although the decrease in the entropy after martensite stabilization is about three times larger for our alloy, which can be related to the change of the magnetic contribution [P3].

Összefoglalás

PhD értekezésem alapvető célja: ferromágneses alakemlékező ötvözetekben zajló martenzites átalakulások vizsgálata különféle zajmérési technikák alkalmazásával. Az átalakulás során a martenzit és az ausztenit közötti határfelület mozgása megindul-megáll jellegű, és így különféle zajok, termikus, akusztikus vagy mágneses emissziók, detektálhatók. Ezen zajok elemzése fontos információt szolgáltathat az átalakulás mikroszkópikus természetéről. A fenti zajokat olyan, két ferromágneses alakemlékező ötvözetben vizsgáltam, amelyek ígéretesek alkalmazási szempontból. A mintákat együttműködő partnereink, Texas Univesity, USA, valamint Tomsk University, Russia, készítették

A) $Ni_{45}Co_5Mn_{36.6}In_{13.4}$ egykristály:

Ez egy speciális, un. meta-mágneses, ferromágneses alakemlékező ötvözet, amelyben nagy telítési mágnesezettség különbség van a ferromágneses ausztenit és a gyengén mágneses martenzit fázisok között. Ezek az ötvözetek nagyon ígéretesek mozgás-átalakítókként (aktuátorokként), vagy (magnetokalorikus tulajdonságuk alapján) mágneses hűtőberendezésekként. Célom, a mágneses átalakulással együtt zajló, martenzites átalakulás szakaszos jellegének vizsgálata volt különféle zajok mérésével.

Meghatároztam a mágneses permeabilitás görbét és azt kaptam, hogy egy éles átmenet van az ausztenit és a matenzit permeabilitásában. A mérésekből meg tudtam határozni a transzformációs hőmérsékleteket. Szintén megmértem az ausztenit fázis mágnesezési görbéjét szobahőmérsékleten.

A DSC görbéket különböző fűtési/hűtési sebességeknél mértem, és a 0.3 K/min sebesség elég alacsony volt ahhoz, hogy a termikus csúcs kis csúcsokra bomoljon (termikus zaj). A kis eseményszámok miatt 7

ciklust kellett mérnem, hogy elegendő adatot kapjak a statisztikus analízishez. Az energia valószínűségsűrűség függvények egyértelműen hatványfüggvény viselkedést mutattak és a kritikus energia kitevőket háromparaméteres nemlineáris illesztéssel (legkisebb négyzetek módszer) illetve az un. maximum likelihood módszerrel határoztam meg. A kalorimetrikus mérésekből megszerkesztettem a martenzites átalakulás hiszterézis görbéjét (az átalakult martezit térfogathányad hőmérséklet függését) és ez jól egyezett a permeabilitás görbéből meghatározottal. Szimultán vizsgáltam az átalakulás során kibocsátott akusztikus és mágneses zajokat külső, rögzített mágnese tereknél (0-230 mT). Az energia, amplitúdó, időtartam és méret valószínűségsűrűség függvényeket ábrázoltam és csillapított hatványfüggvény viselkedést kaptam. Meghatároztam a kritikus kitevőket és azt kaptam, hogy

A1) A DSC valamint akusztikus és mágneses emissziós mérésekből kapott energia kitevők mérési hibahatáron belül megegyeztek. Ez azt jelzi, hogy a martenzites átalakulás során detektált valamennyi zaj eredete közös: az előrehaladó határfelület diszkrét elmozdulásaihoz köthető [P1, C1, C2].

A2) Az akusztikus és mágneses jelek energia és amplitúdó eloszlásainak kitevői függetlenek a külső mágneses tértől (B=20 és 230 mT közötti tartományban) jelezve, hogy a martenzites átalakulás jellege független B-től ilyen tér értékeknél [P1, C1, C2].

A3) Nulla külső mágneses térben a mágneses zaj-csomagok bipoláris (fel és le irányú) jeleket tartalmaztak. Kis mágnes tér alkalmazásával a mágneses jel aktivitása megnőtt és a jelek egyre inkább unipolárissá váltak (mind fűtés és hűtés során), amit az ausztenit növekvő mágnesezettségével magyaráztunk [P1, C1, C2].

A4) Érdekes módon a fűtéshez, illetve hűtéshez tartozó kitevők megegyeztek, szemben a csoport más ferromágneses SMA-kban kapott eredményeivel. Ez jelzi, hogy a zaj kibocsátást eredményező fő diszkrét események (energia felhalmozódás/relaxáció) mindkét irányban azonosak [P1, C1, C2].

B) $Ni_{51}Fe_{18}Ga_{27}Co_4$ egykristály:

Bizonyos martenzit variáns egyirányú feszültséggel való stabilizációja (feszültség indukált martenzit stabilizáció, SIM-aging) nagyon fontos alkalmazási szempontból. Ez növeli a két-irányú reverzibilis alakemlékező viselkedést magas hőmérsékleteken is, és nagy szuper-rugalmas deformációt vagy gumi-szerű viselkedést (10-14%-ig) eredményezhet martenzites állapotban egyirányú feszültséggel, vagy mágneses térrel vezérelt alkalmazásokban. Érdekes volt megfigyelni, hogy a martenzit stabilizáció hogyan befolyásolja a zajok jellemzőit és az átalakulási entrópiát. Háromtípusú mintán végeztem vizsgálatokat; Kvencselt (gyoshűtött), Asztenit-stabilizált (a gyorshűtött mintát 573 K-en 6 óráig kezelve az ausztenit stabilizációja céljából) és SIM-aged (bizonyos martenizit variánst egyirányú feszültséggel stabilizálva) $Ni_{51}Fe_{18}Ga_{27}Co_4$ egykristály mintákon. Szimultán DSC és akusztikus emissziós méréseket végeztem 10 k/min sebességgel fűtéskor és hűtéskor is. Az átalakulási hőmérsékleteket összevetettem a SIM-aging előtti és utáni esetekben. A DSC mérésekből meghatároztam a termikus hiszterézis görbéket, és az átalakulási entrópiát. Az akusztikus aktivitás elemzéséből meghatároztam az energia kitevőket. Az akusztikus emissziós mérések érdekes információt szolgáltattak az átalakulás szakaszos jellegéről, a martenzit stabilizációnak erre gyakorolt hatásáról. Azt kaptam, hogy

B1) A martenzites stabilizáció (SIM-aging), ahogy az várható volt, az átalakulási hőmérsékleteket felfelé tolta és az előre, illetve visszafelé történő átmenetek kiélesedtek, míg a hiszterézis szélessége megnőtt [P3, P4].

B2) Az akusztikus energia kitevők nem változtak a martenzit öregítés (SIM-aging) hatására [P3].

B3) Martenzit öregítés (SIM-aging) után néhány nagy amplitúdójú/energiájú egyedülálló eseményt figyeltem meg fűtés során és ezek a pontok a kisebb energiákhoz tartozó csúcsokra illesztett eloszlás függvény fölé estek. Ezeket a nagyenergiájú eseményeket a fűtés közbeni fázisátalakuláshoz lehetett rendelni és nagysebességű

határfelület mozgásokkal lehetett azonosítani: ez a sebesség nagyságrendekkel nagyobb lehet, mint a tipikus határfelület sebességek a martenzit öregítés előtt [P3].

B4) Az átalakulási entrópia 35%-al kisebb lett martenzit stabilizáció után és gyakorlatilag nem változott ausztenites stabilizációt követően. Ezek kvalitatív egyezésben vannak az irodalomban nem ferromágneses SMA-kban kapott eredményekkel, bár a martenzit stabilizáció után kapott csökkenés mintegy háromszor nagyobb a mi ötvözetünkben, ami kapcsolatban lehet az entrópiához adódó mágneses járulékkal [P3].

Bibliography

[1] K. Otsuka and X. Ren, *Recent developments in the research of shape memory alloys*, Intermetallics, **7** (1999) 511–528.

[2] C. Naresh, P.S.C. Bose, and C.S.P. Rao, *Shape memory alloys: A state of art review*, *IOP Conference Series:* Materials Science and Engineering **149** (2016) 012054.

[3] D.C. Lagoudas, *Shape Memory Alloys: modeling and engineering applications*, Springer (2008) p. 435.

[4] Cimpriˇc Darjan, univerza v ljubljani, *Shape memory alloys*, 2007.

[5] K. Otsuka, and C.M. Wayman, *shape memory materials*. Cambridge University Press, 1999.

[6] D.E. Hodgson, M.H. Wu, and R.J. Biermann, ASM Handbook Volume 2: Properties and Selection: Nonferrous Alloys and Special-Purpose Materials, ASM International, *Shape memory alloys*, (1990) p. 897-902.

[7] E. Panchenko, E. Timofeeva, A.Eftifeeva, S. Osipovich, N. Surikov, Y. Chumlyakov, G. Gerstein, and H.J. Maier, *Giant rubber-like behavior induced by martensite aging in* $Ni_{51}Fe_{18}Ga_{27}Co_4$ *single crystals.* Scripta Materialia, **162** (2019) 387–390.

[8] E. Panchenko, E. Timofeeva, Y. Chumlyakov, S. Osipovich, A.I. Tagiltsev, G. Gerstein, and H.J. Maier, *Compressive shape memory actuation response of stress-induced martensite aged* $Ni_{51}Fe_{18}Ga_{27}Co_4$ *single crystals*. Materials Science& Engineering A, **746** (2019) 448–455.

[9] Z. Wang, A.M. Korsunsky, *Effect of Temperature on Shape Memory Materials,* Reference Module in Materials Science and Materials Engineering, 2020.

[10] D.L. Beke, L. Daróczi, and T.Y. Elrasasi, *Determination of Elastic and Dissipative Energy Contributions to Martensitic Phase Transformation in Shape Memory Alloys*. Shape Memory Alloys-Processing, Characterization and Applications, (In Tech, 2013) p. 167.

[11] E. Patoor, D.C. Lagoudas, P.B. Entchev, L.C. Brinson, and X. Gao, *Shape memory alloys, Part I: General properties and modeling of single crystals*. Mechanics of Materials, **38** (2006) 391–429.

[12] K.K. Alaneme and E.A. Okotete, *Reconciling viability and cost-effective shape memory alloy options –A review of copper and iron based shape memory metallic systems.* Engineering Science and Technology, **19** (2016) 1582–1592.

[13] Y. Guo, A. Klink, C. Fu, and J. Snyder, *Machinability and surface integrity of Nitinol shape memory alloy*. CIRP Annals-Manufacturing Technology, **62** (2013) 83–86.

[14] H. Scherngell and A.C. Kneissl, *Training and stability of the intrinsic two-way shape memory effect in Ni-Ti alloys*. Scripta Materialia, **39** (1998) 205–212.

[15] T. Niendorf, P. Krooß, C. Somsen, G. Eggeler, Y.I. Chumlyakov, and H.J. Maier, *Martensite aging- Avenue to new high temperature shape memory alloys.* Acta Materialia, **89** (2015) 298–304.

[16] C. Picornell, J. Pons, and E. Cesari, *Stabilisation of martensite by applying compressive stress in Cu-Al-Ni single crystals*. Acta Materialia, **49** (2001) 4221–4230.

[17] V.A. Chernenko, J. Pons, E. Cesari, and I.K. Zasimchuk, *Transformation behaviour and martensite stabilization in the ferromagnetic Co-Ni-Ga Heusler alloy.* Scripta Materialia, **50** (2004) 225–229.

[18] P.M. Kadletz, P. Krooß, Y. Chumlyakov, M.J. Gutmann, W.W. Schmahl, H.J. Maier, and T. Niendorf, *Martensite stabilization in shape memory alloys- Experimental evidence for short-range ordering*. Materials Letters, **159** (2015) 16–19.

[19] A. Eftifeeva, E. Panchenko, Y. Chumlyakov, and H. Jürgen Maier, *Two-way shape memory effect in [001]$_{B2}$-oriented Co-Ni-Al single crystals*. Materials Today Proceedings, **4** (2017) 4789–4796.

[20] E. Panchenko, E.Timofeeva, N.G. Larchenkova, Y. Chumlyakov, A.I. Tagiltsev, H.J. Maier, and G. Gerstein, *Two-way shape memory effect under multi-cycles in [001]-oriented $Ni_{49}Fe_{18}Ga_{27}Co_6$ single crystal.* Materials Science& Engineering: A, **706** (2017) 95–103.

[21] X. Ren and K. Otsuka, *Recent advances in understanding the origin of martensite aging phenomena in shape memory alloys.* Phase Transitions: A Multinational Journal, **69** (1999) 329–350.

[22] X. Ren and K. Otsuka, *Origin of rubber-like behaviour in metal alloys.* Nature, **389** (1997) 579–582.

[23] A. Sozinov, A.A. Likhachev, N. Lanska, and K. Ullakko, *Giant magnetic-field-induced strain in NiMnGa seven-layered martensitic phase.* Applied Physics Letters, **80** (2002)1746–1748.

[24] H.E. Karaca, I. Karaman, B. Basaran, Y. Chumlyakov, and H. J. Maier, *Magnetic field and stress induced martensite reorientation in NiMnGa ferromagnetic shape memory alloy single crystals.* Acta Materialia, **54** (2006) 233–245.

[25] H.E. Karaca, I. Karaman, B. Basaran, D.C. Lagoudas, Y. Chumlyakov, and H.J. Maier, *On the stress-assisted magnetic-field-induced phase transformation in Ni_2MnGa ferromagnetic shape memory alloys*. Acta Materialia, **55** (2007) 4253–4269.

[26] Y.J. Huang, Q.D. Hu, N. Bruno, I. Karaman, and J.G. Li, *Influence of grain boundary on pseudoelasticity in highly-oriented polycrystalline $Ni_{52}Fe_{17}Ga_{27}Co_4$ ferromagnetic shape memory alloy*. Materials Letters, **114** (2014) 11–14.

[27] I. Karaman, H.E. Karaca, B. Basaran, D.C. Lagoudas, Y. Chumlyakov, and H.J. Maier, *Stress-assisted reversible magnetic field-induced phase transformation in Ni_2MnGa magnetic shape memory alloys.* Scripta Materialia, **55** (2006) 403–406.

[28] H.E. Karaca, I. Karaman, B. Basaran, Y. Ren, Y.I. Chumlyakov, and H.J. Maier, *Magnetic field-induced phase transformation in NiMnColn magnetic shape-memory alloys-a new actuation mechanism with large work output.* Advanced Functional Materials, **19** (2009) 983–998.

[29] T. Kihara, X. Xu, W. Ito, R. Kainuma, Y. Adachi, T. Kanomata, and M. Tokunaga, *Magnetocaloric Effects in Metamagnetic Shape Memory Alloys*. Shape Memory Alloys- Fundamentals and Applications, 2017, p. 59.

[30] L. Huang, D.Y. Cong, L. Ma, Z.H. Nie, Z.L. Wang, H.L. Suo, Y. Ren, and Y.D. Wang, *Large reversible magnetocaloric effect in a Ni-Co-Mn-In magnetic shape memory alloy.* Applied Physics Letters, **108** (2016) 032405.

[31] T. Kihara, X. Xu, W. Ito, R. Kainuma, and M. Tokunaga, *Direct measurements of inverse magnetocaloric effects in metamagnetic shape-memory alloy NiCoMnIn.* Physical Review B, **90** (2014) 214409.

[32] M.K. Bolgár, L.Z. Tóth, S. Szabó, Sz. Gyöngyösi, L. Daróczi, E. Panchenko, Y. Chumlyakov, D.L. Beke, *Thermal and acoustic noises generated by austenite/martensite transformation in NiFeGaCo single crystals.* Journal of Alloys and Compounds, **658** (2016) 29-35.

[33] L. Daróczi, E. Piros, L.Z. Tóth, and D.L. Beke, *Magnetic field induced random pulse trains of magnetic and acoustic noises in martensitic single-crystal Ni_2MnGa.* Physical Review B, **96 (**2017) 014416.

[34] M.C. Kuntz and J.P. Sethna, *Noise in disordered systems: The power spectrum and dynamic exponents in avalanche models.* Physical Review B, **62** (2000) 11699–11708.

[35] E.K.H. Salje and K.A. Dahmen, *Crackling noise in disordered materials*. Annual Review of Condensed Matter Physics, **5** (2014) 233–254.

[36] A. Planes, L. Mañosa, and E. Vives, *Acoustic emission in martensitic transformations*. Journal of Alloys and Compounds, **577** (2013) 699-704.

[37] M.K. Bolgár, L.Daróczi, L.Z. Tóth, E. Timofeeva, E. Panchenko, Y. Chumlyakov, D.L. Beke, *Effect of γ precipitates on thermal and acoustic noises emitted during austenite/martensite transformation in NiFeGaCo single crystals.* Journal of Alloys and Compounds, **705** (2017) 840–848.

[38] D.L. Beke, M.K. Bolgár, L.Z. Tóth, and L. Daróczi, *On the asymmetry of the forward and reverse martensitic transformations in shape memory alloys.* Journal of Alloys and Compounds, **741** (2018) 106–115.

[39] L.Z. Tóth, S. Szabó, L. Daróczi, and D.L. Beke, *Calorimetric and acoustic emission study of martensitic transformation in single-crystalline Ni_2MnGa alloys*. Physical Review B, **90** (2014) 224103.

[40] M.C. Gallardo, J. Manchado, F.J. Romero, J.D. Cerro, E.K. Salje, A. Planes, E. Vives, R. Romero, and M. Stipcich, *Avalanche criticality in the martensitic transition of $Cu_{67.64}Zn_{16.71}Al_{15.65}$ shape-memory alloy: A calorimetric and acoustic emission study*. Physical Review B, **81** (2010) 174102.

[41] M.L. Rosinberg and E. Vives, *Metastability, hysteresis, avalanches, and acoustic emission: Martensitic transitions in functional materials*. Springer Series in Materials Science, **148** (2011) 249–272.

[42] R. Niemann, J. Kopeček, O. Heczko, J. Romberg, L. Schultz, S. Fähler, E. Vives, L. Mañosa, and A. Planes, *Localizing sources of acoustic emission during the martensitic transformation*. Physical Review B, **89** (2014) 214118.

[43] Z. Balogh, L. Daroczi, L. Harasztosi, D. Beke, T.A. Lograsso, and D.L. Schlagel, *Magnetic emission during austenite-martensite transformation in Ni2MnGa shape memory alloy*. Materials Transactions, **47** (2006) 631-634.

[44] J. Baró, S. Dixon, R.S. Edwards, Y. Fan, D.S. Keeble, L. Mañosa, A. Planes, and E. Vives, *Simultaneous detection of acoustic emission and Barkhausen noise during the martensitic transition of a Ni-Mn-Ga magnetic shape-memory alloy*. Physical Review B, **88** (2013) 174708.

[45] L. Daróczi, S. Gyöngyösi, L.Z. Tóth, S. Szabó, and D.L. Beke, J*erky magnetic noises generated by cyclic deformation of martensite in Ni_2MnGa single crystalline shape memory alloys*. Applied Physics Letters, **106** (2015) 041908.

[46] L.Z. Tóth, L. Daróczi, S. Szabó, and D.L. Beke, *Simultaneous investigation of thermal, acoustic, and magnetic emission during martensitic transformation in single-crystalline Ni_2MnGa*. Physical Review B, **93** (2016) 144108.

[47] L.Z. Tóth, Fázisátalakulást kísérő zajok vizsgálata Ni_2MnGa alakemlékező ötvözet ekben, Debreceni Egyetem, 2018.

[48] N.E. Barta and I. Karaman, *Embedded magnetic shape memory sensory particles in lightweight composites for crack detection*. Material Science and Engineering A, **751** (2019) 201–213.

[49] T.Y. Elrasasi, M.M. Dobróka, L. Daróczi, and D.L. Beke, *Effect of thermal and mechanical cycling on the elastic and dissipative energy in CuAl(11.5wt%)Ni(5.0wt%) shape memory alloy*. Journal of Alloys and Compounds, **577** (2013) S517–S520.

[50] E.P. White, B.J. Enquist, and J.L. Green, *On estimating the exponent of power-law frequency distributions*. Ecology **89** (2008) 905–912.

[51] E.K.H. Salje, A. Planes, and E. Vives, *Analysis of crackling noise using the maximum-likelihood method: Power-law mixing and exponential damping*. Physical Review E, **96** (2017) 042122.

[52] M.K. Bolgár, L. Daróczi, L.Z. Tóth, E.Timofeeva, E. Panchenko, Y. Chumlyakov, D.L. Beke, *Magnetic noises emitted during martensitic transformation in $Ni_{49}Fe_{18}Ga_{27}Co_6$ single crystalline shape memory alloys*. Intermetallics, **107** (2019) 103–107.

[53] S. Kustov, I. Golovin, M.L. Corró, and E. Cesari, *Isothermal martensitic transformation in metamagnetic shape memory alloys*. Journal of Applied Physics, **107** (2010) 053525.

[54] J. Baró, K.A. Dahmen, J. Davidsen, A. Planes, P.O. Castillo, G.F. Nataf, E.K.H. Salje, and E. Vives, *Experimental Evidence of Accelerated Seismic Release without Critical Failure in Acoustic Emissions of Compressed Nanoporous Materials.* Physical Review Letters, **120** (2018) 245501.

[55] E. Bonnot, L. Mañosa, A. Planes, D.S. Parra, E. Vives, B. Ludwig, C. Strothkaemper, T. Fukuda, and T. Kakeshita, *Acoustic emission in the fcc-fct martensitic transition of* $Fe_{68.8}Pd_{31.2}$. Physical Review B, **78** (2008) 184103.

[56] R. Kainuma, Y. Imano, W. Ito, Y. Sutou, H. Morito, S. Okamoto, O. Kitakami, K. Oikawa, A. Fujita, T. Kanomata, and K. Ishida, *Magnetic-field-induced shape recovery by reverse phase transformation*. Nature, **439** (2006) 957–960.

[57] R. Y. Umetsu, W. Ito, K. Ito, K. Koyama, A. Fujita, K. Oikawa, T. Kanomata, R. Kainuma, and K. Ishida, *Anomaly in entropy change between parent and martensite phases in the* $Ni_{50}Mn_{34}In_{16}$ *Heusler alloy*. Scripta Materialia, **60** (2009) 25–28.

[58] H.B. Huang, X.Q. Ma, J.J. Wang, Z.H. Liu, W.Q. He, and L.Q. Chen, *A phase-field model of phase transitions and domain structures of NiCoMnIn metamagnetic alloys.* Acta Materialia, **83** (2015) 333–340.

[59] D.L. Beke, L. Daróczi, N.M. Samy, L.Z. Tóth, and M.K. Bolgár, *On the thermodynamic analysis of martensite stabilization treatments.* Acta Materialia, **200** (2020) 490-501.

[60] J. Marcos. A. Planes, L. Mañosa, F. Casanova, X. Batlle, A. Labarta, B. Martínez, *Magnetic field induced entropy change and magnetoelasticity in Ni-Mn-Ga alloys*. Physical Review B, **66** (2002) 224413.

[61] D.L. Beke, L. Daróczi, L.Z. Tóth, M.K. Bolgár, N.M. Samy, and A. Hudák, *Acoustic emissions during structural changes in shape memory Alloys*. Metals, **9** (2019) 58.

[62] E. Bonnot, E. Vives, L. Mañosa, A. Planes, and R. Romero, *Acoustic emission and energy dissipation during front propagation in a stress-driven martensitic transition*. Physical Review B, **78** (2008) 094104.

[63] N. Zreihan, E. Faran, E. Vives, A. Planes, and D. Shilo, *Relations between stress drops and acoustic emission measured during mechanical loading*.Physical Review Materials, **3** (2019) 043603.

[64] R. Santamarta, E. Cesari, J. Font, J. Muntasell, J. Pons, and J. Dutkiewicz, *Effect of atomic order on the martensitic transformation of Ni-Fe-Ga alloys*. Scripta Materialia, **54** (2006) 1985–1989.

[65] M. Chandrasekaran, L. Cooreman, J. Van Humbeeck, and L. Delaey, *Martensitic transformation in CuZnAl: Changes in transformation entropy due to post quench ageing in the β or martensitic condition*. Scripta Metallurgica, **23** (1989) 237–239.

[66] C. Seguí and E. Cesari, *Contributions to the transformation entropy change and influencing factors in metamagnetic Ni-Co-Mn-Ga shape memory alloys*. Entropy, **16** (2014) 5560–5574.

[67] V.V. Khovailo, K. Oikawa, T. Abe, and T. Takagi, *Entropy change at the martensitic transformation in ferromagnetic shape memory alloys $Ni_{2+x}Mn_{1-x}Ga$*. Journal of Applied Physics, **93** (2003) 8483–8485.

[68] M. Ahlers and J.L. Pelegrina, *Ageing of martensite: Stabilisation and ferroelasticity in Cu-based shape memory alloys*. Materials Science and Engineering A, **356** (2003) 298–315.

[69] S. Kustov, J. Pons, E. Cesari, and J. Van Humbeeck, *Chemical and mechanical stabilization of martensite*. Acta Materialia, **52** (2004) 4547–4559.

List of Publications

1- Publications related to the dissertation

P1. **N.M. Samy**, M.K. Bolgar, N. Barta, L. Daroczi, L.Z. Toth, Y. Chumlyakov, I. Karaman, D.L. Beke: *Thermal, acoustic and magnetic noises emitted during martensitic transformation in single crystalline* $Ni_{45}Co_5Mn_{36.6}In_{13.4}$ *meta-magnetic shape memory alloy*, Journal of Alloys and Compounds **778** (2019) 669-680.

Cited by (3)
IF: 4.65

P2. D.L. Beke, L. Daroczi, L.Z. Toth, M.K. Bolgar, **N.M. Samy**, Anikó Hudák: *Acoustic Emissions during Structural Changes in Shape Memory Alloys*, Metals **9** (2019) 58.

Cited by (6)
IF: 2.117

P3. **N.M. Samy**, L. Daroczi, L.Z. Toth, Elena Panchenko, Y. Chumlyakov, N. Surikov, D.L. Beke: *Effect of Stress-Induced Martensite Stabilization on Acoustic Emission Characteristics and the Entropy of Martensitic Transformation in Shape Memory* $Ni_{51}Fe_{18}Ga_{27}Co_4$ *Single Crystal*, Metals **10** (2020) 534.

Cited by (3)
IF: 2.117

P4. D.L. Beke, L. Daróczi, **N.M. Samy**, L.Z. Tóth, M.K. Bolgár: *On the thermodynamic analysis of martensite stabilization treatments*, Acta Materialia **200** (2020) 490–501.

Cited by (2)
IF: 7.656

2- Other publications

P5. N. M. Samy, S.S. Shenouda, M. Fadel, H. Talaat, G.L. Katona, G.A. Langer, A. Csik & D.L. Beke: *Investigation of solid-state reaction in Ag/Sn nanostructured thin films at room temperature*, Philosophical Magazine **95** (2015) 2990-3001.

Cited by (5)
IF: 1.632

Conferences

C1. Presentation in “DOFFI, Balaton fenyves, Magyarország, 2018.06.15-18.

N.M. Samy, M.K. Bolgar, N. Barta, L. Daroczi, L.Z. Toth, Y. Chumlyakov, I. Karaman, D.L. Beke,

Title: Noisy Character of Phase Transformations in $Ni_{45}Co_5Mn_{36.6}In_{13.4}$ Single Crystal

C2. Poster in European Symposium on Martensitic Transformations (ESOMAT 2018), Metz, France, 2018.08.27-31.

N.M. Samy, M.K. Bolgar, N. Barta, L. Daroczi, L.Z. Toth, Y. Chumlyakov, I. Karaman, D.L. Beke,

Title: Thermal, acoustic and magnetic noises emitted during martensitic transformation in $Ni_{45}Co_5Mn_{36.6}In_{13.4}$ meta-magnetic shape memory alloy single crystals

Acknowledgments

First of all, I express my thanks and gratitude to my God for helping me to complete this work with success.

I am deeply indebted to my supervisor Prof. Dr. Dezső L. Beke who was always standing with me and did a great effort with me. It was a great opportunity in my life to be his PhD student. He always followed my experimental results, discussing and explaining the physics behind them. Because of his guidance, valuable scientific comments, and ideas, I was able to reach good results. I had learned a lot from his interesting lectures, discussions, writing my publications, and revising the dissertation. I had learned a lot from him, not only on the scientific level but also on the human level. He is a kind father, guidance character, expert physicist, and a great professor. Thanks to his warm family.

I'm extremely grateful to Dr. Lajos Daróczi for his absolute help. We had spent a lot of time during which we did a lot of experiments. He was kind, helpful, and patient to explain to me everything. He is an excellent expert in developing experimental systems, I learned a lot from him. I enjoyed discussing the results with him and solving the experimental problems during the measurements. Even he was always helping with other things that I needed.

I would like to thank my colleagues in the work team. Thanks to László Z. Tóth for his help to understand and use the program for the statistical evaluation of the data, his advice, valuable comments, and helping in everything. Thanks to Melinda Bolgár who started with me; taught me how to use the experimental techniques, understanding a lot of things behind the research, and supported me.

Thanks to our partner Prof. Dr. Ibrahim Karaman in Texas A&M University, United States, and Prof. Dr. Elena Panchenko in Tomsk State University, Russia for providing us the samples.

I express my gratitude to the Department of Solid State Physics-Faculty of Science and Technology, Debrecen University in Hungary. My sincere thanks go to Prof. Zoltán Erdélyi, the head of the Department, and Prof. Dr. Ferenc Kun, the head of the Doctoral School of Physics.

Thanks to the administrative staff of the Department; Katalin Bakóné Kósa, Judit Csikós, and Évá Kosztyuné Gottfried for their continuous help. Thanks to all the administrative staff of the University of Debrecen

Thanks to the Doctoral School and the Doctoral Council. Thanks to Dr. László Olah and Bessenyei Éva for their help. I would like to deeply thank Dr. Dorottya Sohler who made a great effort to follow, check, and finalize my PhD procedure, explaining to me everything to do.

Thanks to all the co-workers in the department for helping me. Thanks to all my Hungarian friends and colleagues for their help.

Thanks to the Hungarian Scholarship Board (HSB). Thanks to the Ministry of Higher Education and Scientific Research in Egypt and the Egyptian Culture Office in Vienna. Thanks to Prof. Dr. Amr Elatraby, Prof. Dr. Ola Abdelgawad, Dr. Anna Diltsch, Olaf, and all the members of the Egyptian Culture Office for their continuous help and support.

Thanks to my referees. I greatly appreciate their excellent insights.

Finally, thanks to my parents, brothers, and sisters for their continuous encouragement and supporting me all the time.

This work was supported by the GINOP-2.3.2-15-2016-00041 project. The project was co-financed by the European Union and the European Regional Development Fund. The described research was also supported through the National Research, Development, and Innovation Office-NKFIH K119566 project.